	VIRGO NOTE Virgo Input Mirrors thermal effects characterization	Date 17/03/2010 VIR-0191A-10 page : Page 1 of 33
--	--	--



Virgo Input Mirrors thermal effects characterization

VIR-0191A-10

R. Day, V. Fafone, J. Marque, M. Pichot, M. Punturo, A. Rocchi

17/03/2010



Summary


1. Introduction.....	2
2. Thermal lensing with respect to absorption.....	3
3. Optical Transfer Functions.....	4
4. Spatial amplitude distribution of the Side-Bands at the dark port.....	9
5. CO2 ring correction	12
5.1. Estimation of the lensing created by the heating annulus.....	12
5.2. Comparison of ANSYS results with phase camera measurements.....	14
6. BS pick-off beam size and phase camera measurements.....	15
6.1. Introduction.....	15
6.2. Phase camera measurement	15
6.2.1. Configuration A:.....	16
6.2.2. Configuration B:.....	17
6.2.3. Measuring Thermal Lens	18
6.2.4. ITF cool-down to determine input mirror lensing.....	18
6.2.5. Calculating absorption.	19
6.3. Beam Size Measurement.....	20
6.3.1. Calibrating with CO2 ring	21
6.3.2. ITF cool-down to determine input mirror lensing.....	21
6.3.3. Calculating absorption.	22
6.4. Conclusion	23
7. Mirror absorption measurement through the bulk temperature measurement with the resonant mode technique.....	23
7.1. The resonant mode method.....	23
7.2. Verification of the calibration.....	25
7.3. Opto-Thermal finite element modeling of the mirror.....	26
7.4. Absorption measurement	26
8. Conclusions.....	30
9. References.....	31
10. Annex.....	32

1. Introduction

The scope of this document is to summarize all methods and results obtained in order to characterize the thermal lensing effect observed in the Input Mirrors (IMs) of Virgo. An extensive analytical model has been published by Jean-Yves Vinet in [1].

This characterization is of first importance since we have experienced that this effect is a show-stopper for further increasing the power inside the arms of Virgo. Indeed, the main consequence is the degeneracy of the sidebands in the recycling cavity leading to instabilities of the longitudinal and alignment error signals (or spurious extra offsets) preventing the lock acquisition (or affecting the stability and/or noise performance).

As a first step, it is described how the thermo-optic effect is modeled in chapter 2, comparing the analytic model with a simulation.

	<p style="text-align: center;">VIRGO NOTE Virgo Input Mirrors thermal effects characterization</p>	<p>Date 17/03/2010 VIR-0191A-10 page : Page 3 of 33</p>
--	--	---

Chapter 3 to 6 describes 5 different techniques to measure optically the lensing effect in Virgo. Chapter 7 describes a technique to measure the change of temperature of the IMs giving some estimation of their absorption.

Chapter 8 summarizes all the results, highlighting the limitations of these studies but also the remaining not understood conclusions.

2. Thermal lensing with respect to absorption

In the following, we used an ANSYS 2D axi-symmetrical simulation to calculate the optical path length (OPL) for different values of the power absorbed in the coating, considering the thermo-optic effect (change of the refractive index with the temperature) and the thermo-elastic deformation of the test mass (the elasto-optic term, due to the change of the refractive index induced by the mechanical strain, has been neglected, being of the order of 1% with respect to the other contributions).

For each OPL, we computed the focal length by fitting the OPL with Gaussian weights. The equation for the fit is $OPL(r) = \frac{1}{2F}r^2 + c$, where F is the focal length in meters. The weighting Gaussian is $f(r) = \frac{1}{\pi w^2} e^{-\frac{2r^2}{w^2}}$, where $w=0.0215m$. At last, we plotted the resulting focal lengths as a function of the absorbed power and fitted them with the function $F(P) = \frac{\psi}{P}$.

First of all, we performed a crosscheck between ANSYS and the Hello-Vinet analytical steady state solution (see Virgo Physics Book Vol. II, pages 289-301), considering only the thermo-optic effect. The result of the fit is shown in Figure 2.1, where the good agreement is evident since the two curves are very well superposed. A value of $\psi=418m \cdot W$ is derived for both calculations.

Then, we used the ANSYS temperature maps to calculate the OPL considering both thermo-optic and thermo-elastic effects, so in the calculation of the OPL, the term

$$\alpha(n-1)(\sigma+1) \int \Delta T(r,z) dz$$

has been added. The results, comparing the cases without and with thermo-elastic effect, are shown in Figure 2.2. In the latter case a value of $\psi=405m \cdot W$ is derived. In the following paragraph a n error of 13% will be assumed on this value due to the uncertainty on the dn/dT value at 1064nm.

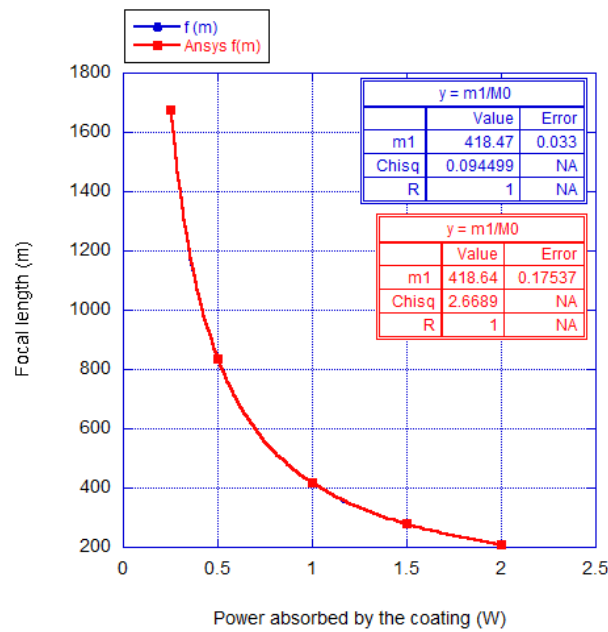


Figure 2.1: Thermal lens focal length as a function of the absorbed power for the analytical calculation (blue curve) and ANSYS simulation (red curve). The two plots are superposed.

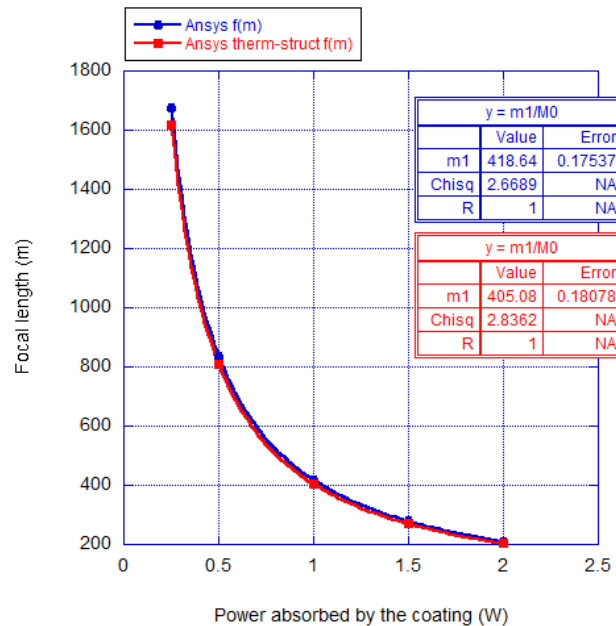


Figure 2.2: Thermal lens focal length as a function of the absorbed power for the case of thermo-optic effect only (blue curve) and the sum of thermo-optic and thermo-elastic effects (red curve) obtained from the ANSYS simulations.

3. Optical Transfer Functions

Beginning of 2009, the dependence between the SSFS optical TF (Transfer function between SSFS correction and B5_ACp) and thermal effects has been put in evidence, by measuring this TF with different TCS powers. Figure 3.1 shows how the TF changes depending on the power of the TCS rings on NI and WI mirrors.

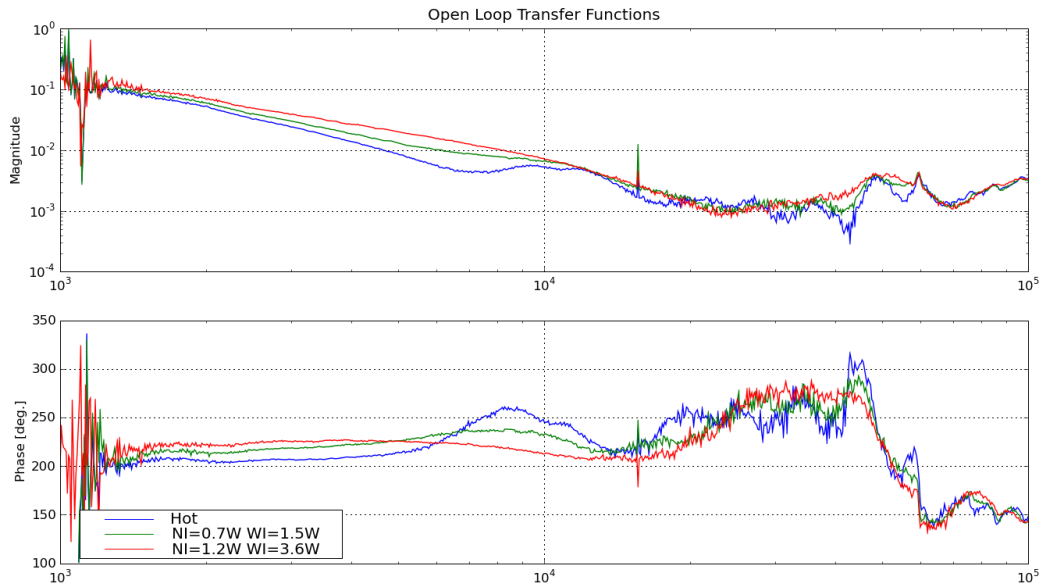


Figure 3.1: Measurement of SSFS optical TF for different TCS ring powers

This was quite a bad surprise for the commissioning of the interferometer since we found out that the SSFS loop required different analogic filtering for a “hot interferometer” and for a “cold interferometer”. However, this is the opportunity to “measure” the thermal effects. Obviously, the measurement is quite indirect since the TF was found to be dependant on a long list of parameters (all are common parameters of the interferometer): operating point of PRCL and CARM, macroscopic length of PRCL and arms, frequency of modulation, radius of curvatures, losses in the arms, finesse of the arms and lensing in the input mirrors. Anyway, it should provide a rough estimation.

A simulation with Finesse was set up to reproduce the SSFS optical TF. The thermal lensing effect has been simply simulated by inserting a thin lens of adjustable focal length inside the Input Mirrors substrate.

It was actually possible to roughly fit the measurement at 8W input power without TCS (see Figure 3.2) with a 15km focal length with an error of +/-2km. Assuming the lensing follows the law $f=405/P_{abs}$ (in meter, +/-13%, see chapter 2), the power absorbed is 27mW +/-20%.

Assuming the power stored in the Fabry-Perot cavity is $P_{cav} = \frac{P_{in} G_{rec} \mathcal{F}}{\pi}$ within +/-15% (10% error on G , 5% error on input power), where $G_{rec} = 45$ [8] is the recycling gain and $\mathcal{F} = 50$ is the arm cavity finesse, the average absorption of the IMs’ HR coating is 4.7ppm +/-25%.

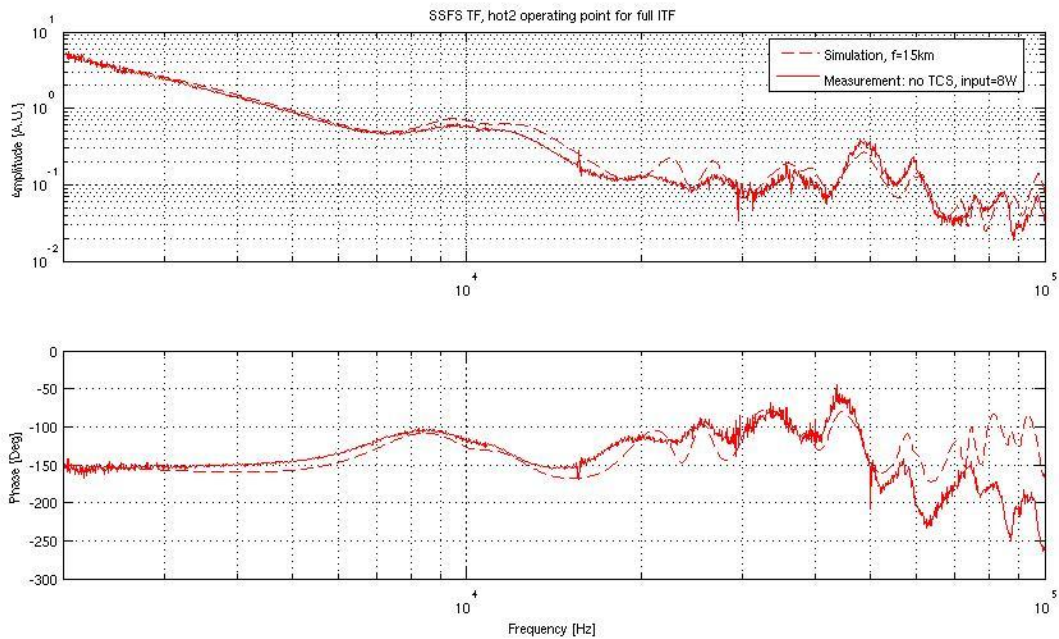


Figure 3.2: Simulation of SSFS TF with 15km focal length in IM is best fitting the measurement of SSFS TF with 8W ITF input power.

The TF has also been measured later with high TCS corrections (4W on WI, and 3W on NI, +/- 10%) and an input power of 17W. Figure 3.3 shows that, in these conditions, the thermal effects have been quite well corrected since the measured TF is matching the one expected with the simulation when there is no lensing in the Input Mirrors within an error of $\pm 3 \cdot 10^{-5}$ dpt. Assuming the lensing created by the ring is $-2.7 \cdot 10^{-5}$ dpt/ W_{CO_2} +/- 20% (see chapters 5 and 6), the thermal lensing created by the YAG is $0.95 \cdot 10^{-4}$ dpt +/- 37% or a power absorbed of 38.5mW +/- 40%. This leads to the IM's coating absorption of 3.2ppm +/- 41%.

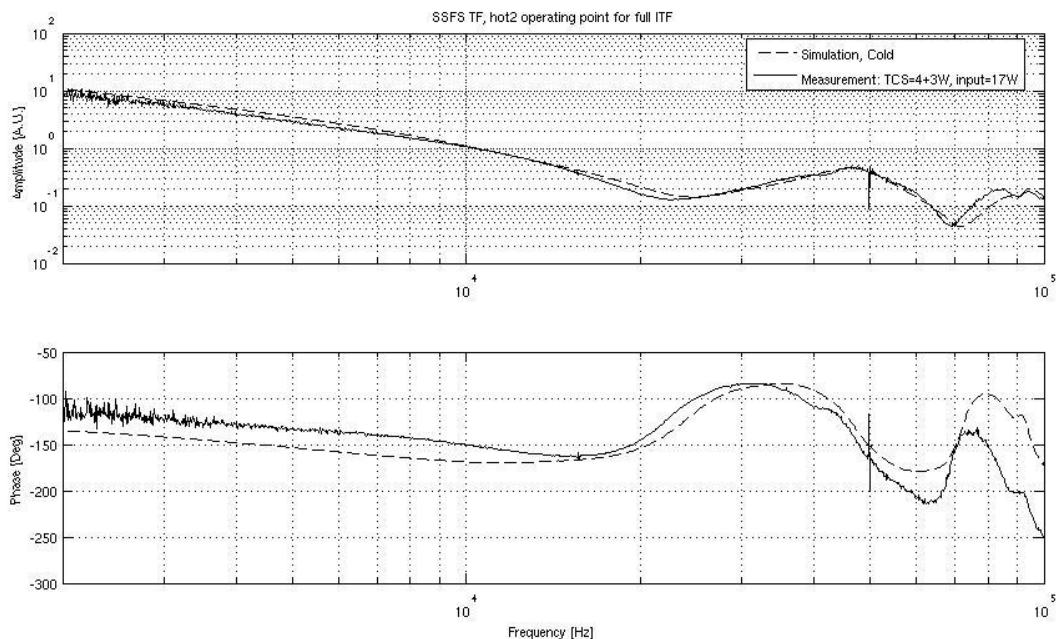


Figure 3.3: Simulation of SSFS TF cold state is best fitting the measurement of SSFS TF with 17W ITF input power and a correction of 4 and 3W of TCS.

One characteristic of this TF is the notch expected at the frequency of the Free Spectral Range of the arms (around 50kHz). This has been measured at 17W input power (and 1W TCS correction on each Input Mirror, +/-10%) several times to check its stability (Figure 3.4). The notch was expected exactly at 49967Hz (assuming the length of the arms is 2999.9m) and very deep. It was not the case, and, once again, the shape in amplitude and phase of the notch was found to be very dependent on all common parameters of the interferometer. A tuning of the simulation was done to best fit the measurement (see Figure 3.5): a thermal lens of 17km +/-2km was introduced in the simulation. Assuming the lensing created by the ring is $-2.7 \cdot 10^{-5}$ dpt/W_{CO2} +/-20% (see chapters 5 and 6), the thermal lensing created by the YAG is $0.86 \cdot 10^{-4}$ dpt +/-20% or a power absorbed of 35mW +/-26%. This leads to the IM's coating absorption of 2.9ppm +/-29%.

Finally, Figure 3.6 shows as the TF around 50kHz is sensitive with respect to different lensing in the Input Mirrors.

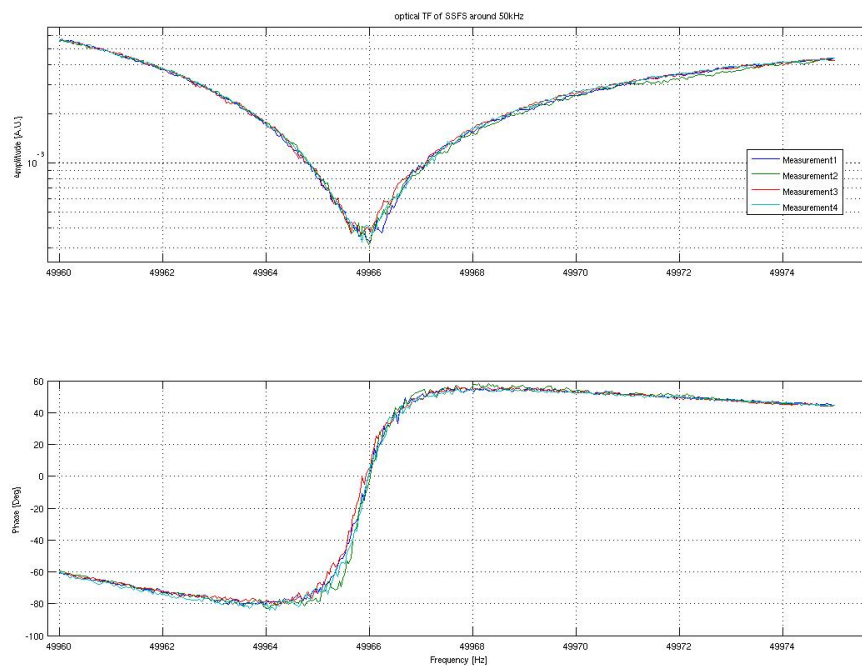


Figure 3.4: Measurement of SSFS TF around 50kHz with 17W ITF input power and a TCS correction of 1W on each Input Mirror.

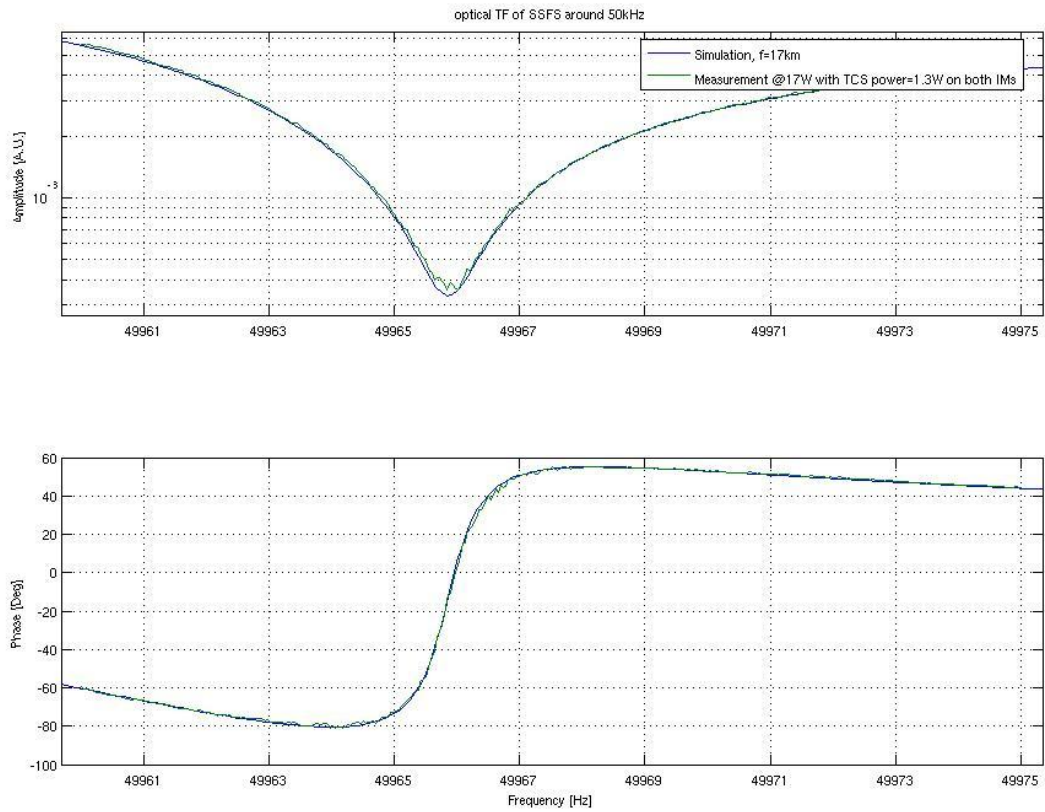


Figure 3.5: Simulation and measurement of SSFS TF around 50kHz with 17W ITF input power and a TCS correction of 1W on each Input Mirror.

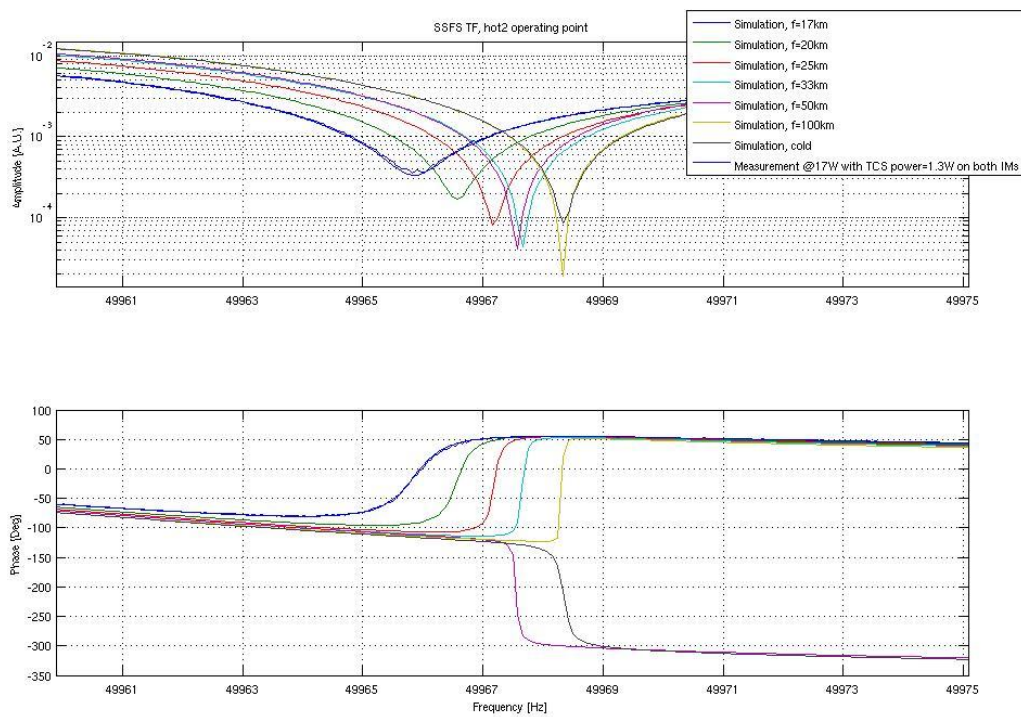


Figure 3.6: Simulations of SSFS TF around 50kHz with different lensing in the Input Mirrors.

4. Spatial amplitude distribution of the Side-Bands at the dark port

Many tests have been carried out with the TCS before VSR2 to optimize the thermal correction effect in the Input Mirrors. The amplitude images of the sidebands at the anti-symmetric port as measured with the Phase Camera have been used to tune the correction powers of the rings on the NI and WI mirrors. A simulation done with Finesse has been carried out to reproduce the images of the sidebands and give some hints for guessing the final tuning to achieve.

Figure 4.1 shows the starting point: 13W input power, the sidebands images are quite “aberrated” and the images are well reproduced with the simulation by adding a lensing effect of 8km in each input mirror within an error of +/-2km (the error is estimated by visual appreciation of the images). Assuming the lensing follows the law $f=405/\text{Pabs}$ (in meter, +/-13%, see chapter 2), the power absorbed is 49mW +/-28%. Again, assuming the power stored in the Fabry-Perot cavity is $P_{cav} = \frac{P_{in} G_{rsc} \mathcal{F}}{\pi}$ +/-15%, the average absorption of the IMs’ HR coating is 5.3ppm +/- 32%.

Figure 4.2 and 4.3 show what happens if some correction is applied only on one mirror: essentially the Upper Side-Band spot size decreases when correction is applied only on WI mirror while the Lower Side-Band spot size decreases when correction is applied only on NI.

This helped to tune the differential power applied on both mirrors while the common power was tuned so that the Side-Bands spot size was judged to be the right one (the same than measured when the PR mirror is not aligned).

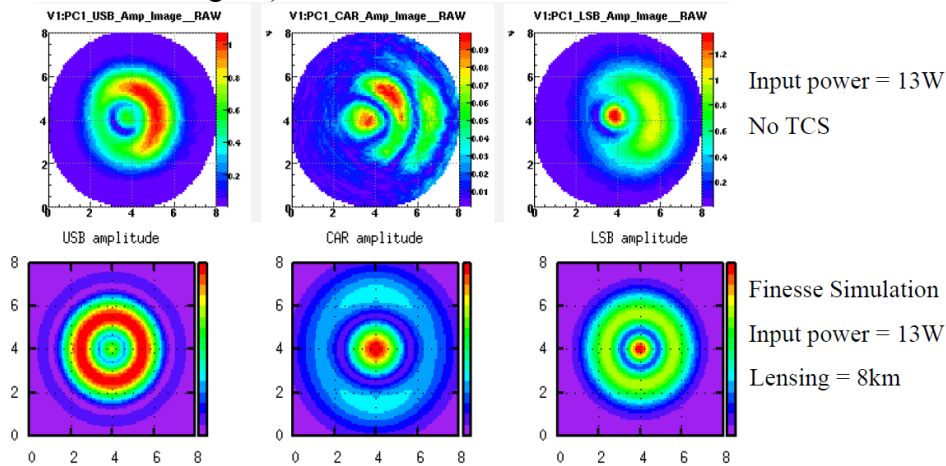


Figure 4.1: Amplitude of the sidebands and carrier fields at the anti-symmetric port with no TCS correction (first row: as measured by the phase camera, second row: output of a Finesse simulation)

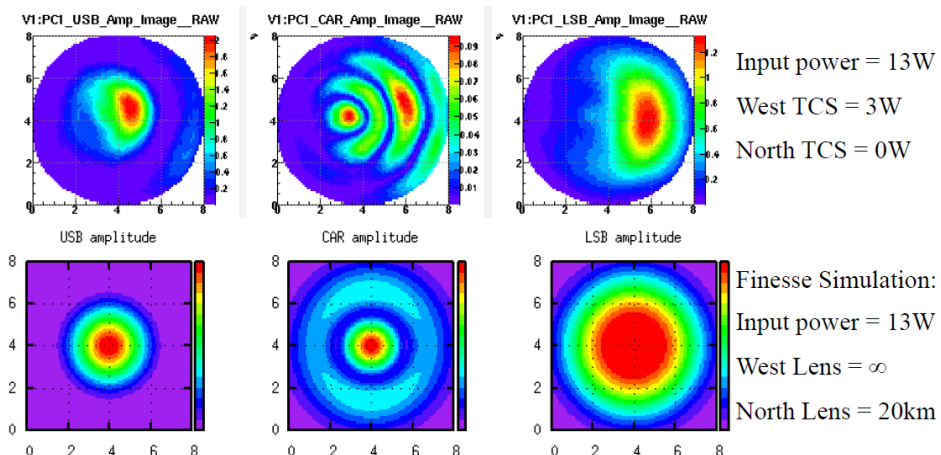


Figure 4.2: Amplitude of the sidebands and carrier fields at the anti-symmetric port with TCS correction only on WI mirror (first row: as measured by the phase camera, second row: output of a Finesse simulation)

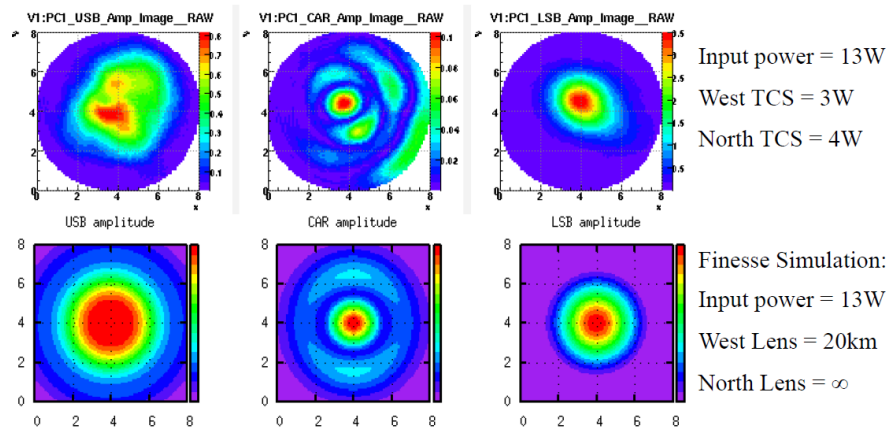


Figure 4.3: Amplitude of the sidebands and carrier fields at the anti-symmetric port with TCS correction only on NI mirror (first row: as measured by the phase camera, second row: output of a Finesse simulation)

The best tuning with 17W input power was achieved with 6.5W on the WI and 4W on the NI (see Figure 4.4). This result has been obtained by optimizing the TCS powers within 0.5W. Assuming the lensing created by the ring is $-2.7 \cdot 10^{-5}$ dpt/W_{CO2} +/-20% (see chapters 5 and 6), the thermal lensing created by the YAG is $1.1 \cdot 10^{-4}$ dpt +/-30% for the NI and $1.8 \cdot 10^{-4}$ dpt +/-22% for the WI. This leads to the IM's coating absorption of 3.6ppm for the NI and 5.8ppm +/-31% for the WI.

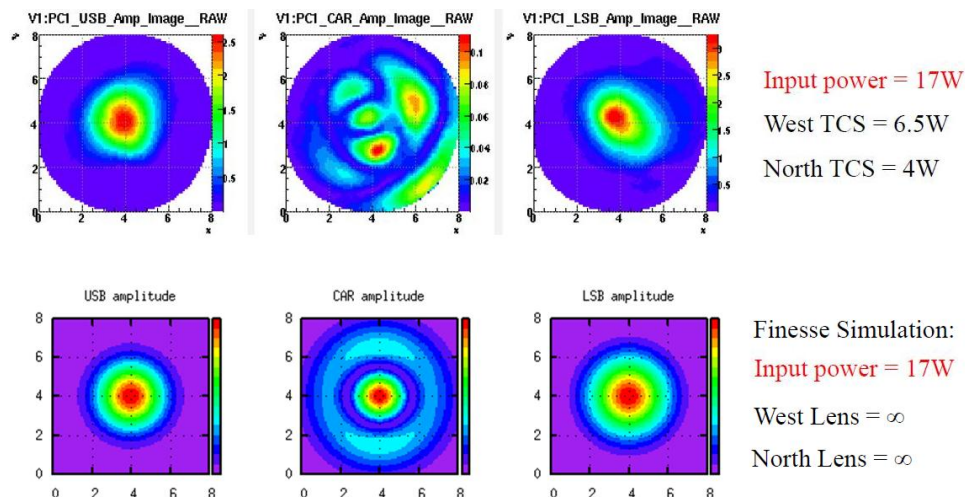


Figure 4.4: Amplitude of the sidebands and carrier fields at the anti-symmetric port with TCS correction optimized on both input mirrors (first row: as measured by the phase camera, second row: output of a Finesse simulation without thermal effects)

Figure 4.5 gives an idea of how the shape of the sidebands changes as the lensing increases. This kind of simulation has also been achieved with the FFT propagation simulation DarkF. There is a fairly good agreement between both kinds of simulations which is quite satisfactory because not only the principle of calculation is different but also the way thermal effects are simulated: in Finesse, the thermal effects are modeled with a single thin lens in the Input Mirrors substrate, while in DarkF the optical fields going through the Input Mirrors substrate are affected by a “corrective map” entirely analytically computed just on the base of the power absorbed by the HR coating [1].

Figure 4.7 gives the phase camera images at step1 of the lock acquisition scheme (power recycling mirror is misaligned). Figure 4.8 gives the phase camera images at step6, just 1s after the dark fringe has been reached (significant thermal effects started 1s before this image was shot).

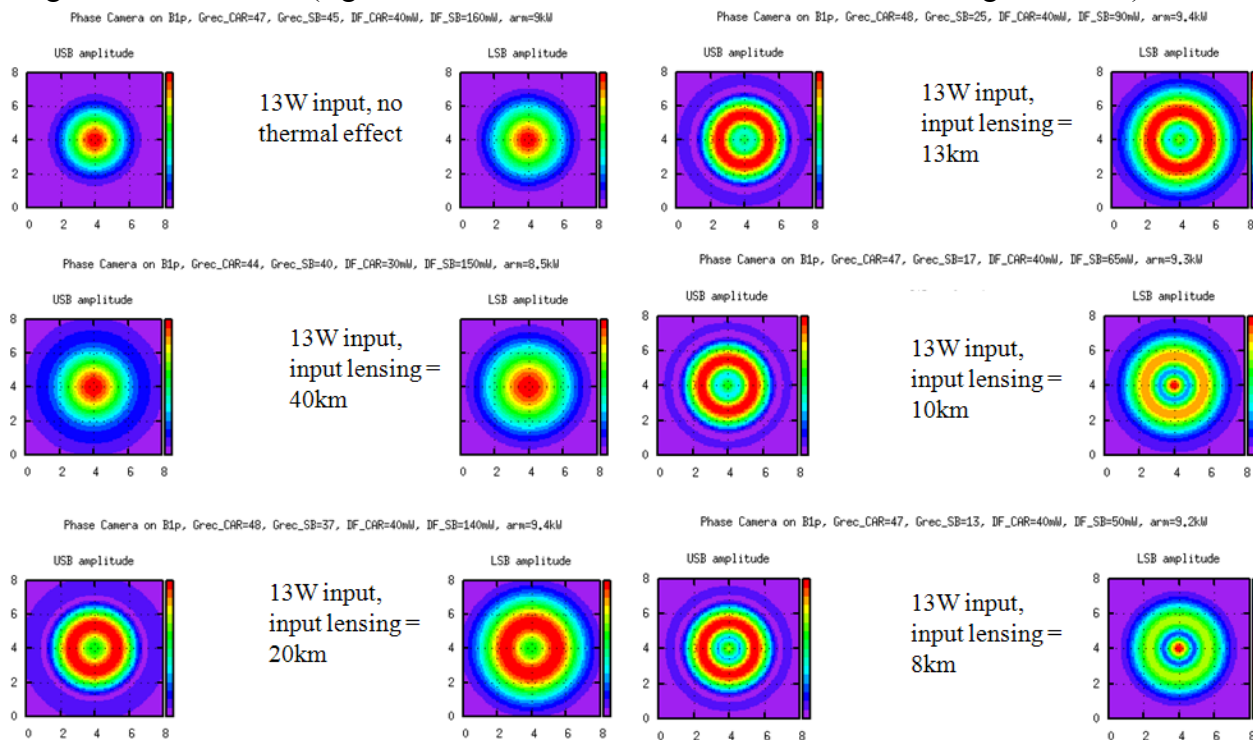


Figure 4.5: Amplitude of the sidebands at the anti-symmetric port with different lensing (Finesse simulation)

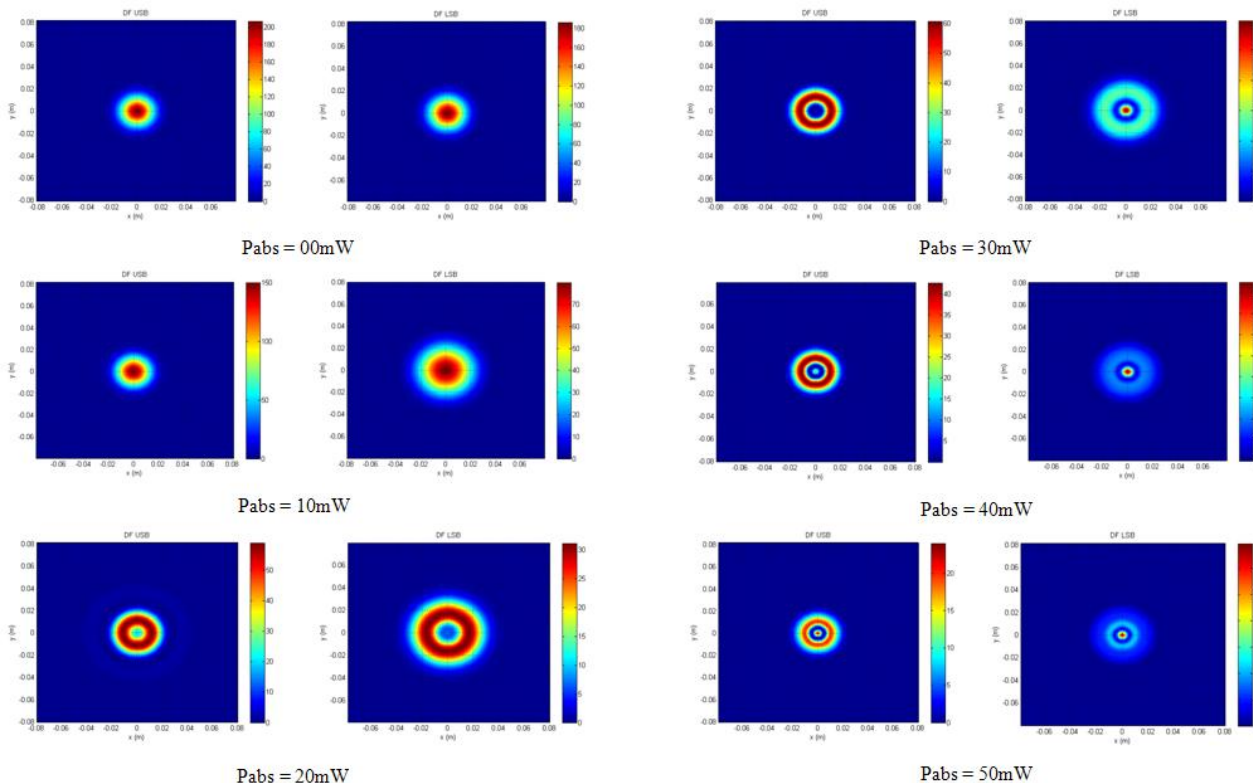


Figure 4.6: Amplitude of the sidebands at the anti-symmetric port with different power absorbed by the HR coating (DarkF simulation)

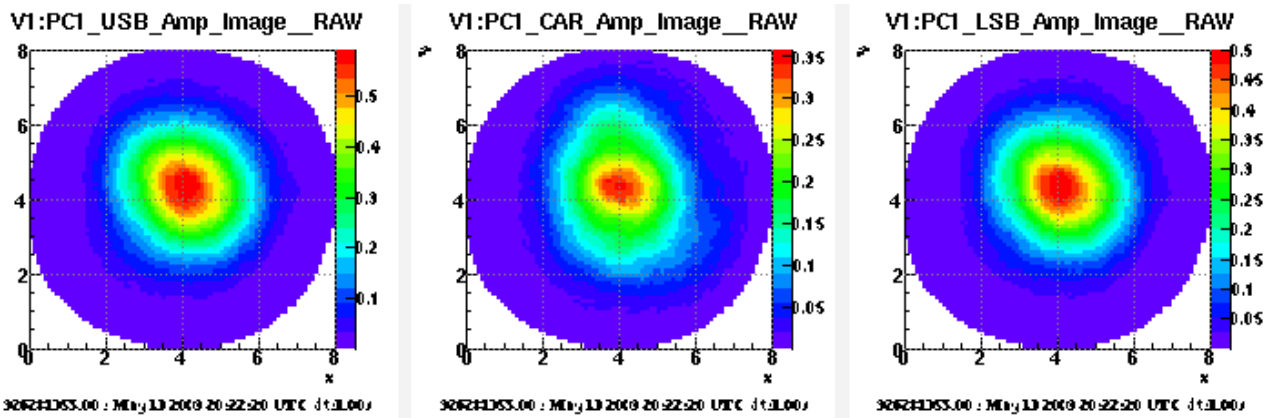


Figure 4.7: Phase camera images at step1

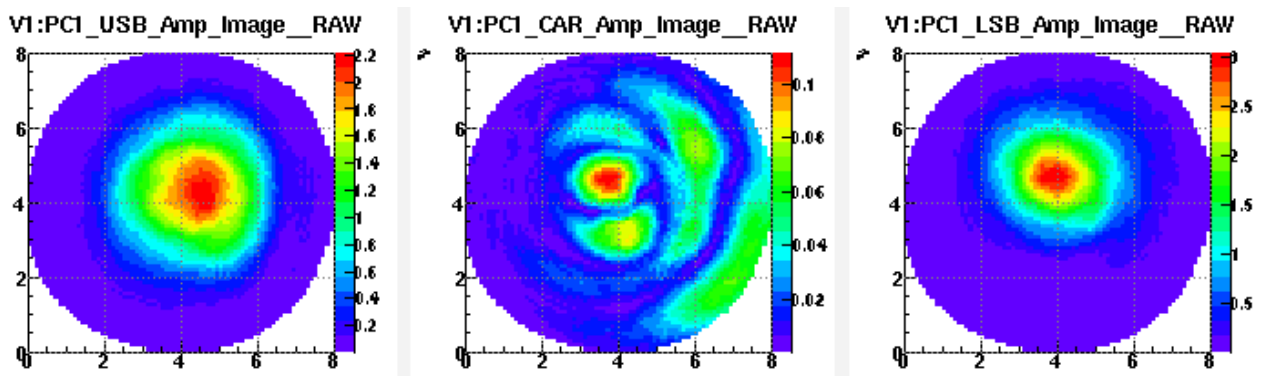


Figure 4.8: Phase camera images at step6, 1 second after the thermal effects have started

5. CO₂ ring correction

5.1. Estimation of the lensing created by the heating annulus

The TCS telescope images onto the ITM an annular pattern created by an AXICON. To check the quality and measure the size of the heating annulus, a paper screen is placed on the image plane of the TCS telescope. From the picture recorded by a thermal camera behind the screen, using an object with known dimensions, it is possible to measure the size of the annulus (see Figure 5-1). This annulus is in place on each bench since January 2009 (the NI ring was changed on October 2009 after the CO₂ laser replacement).

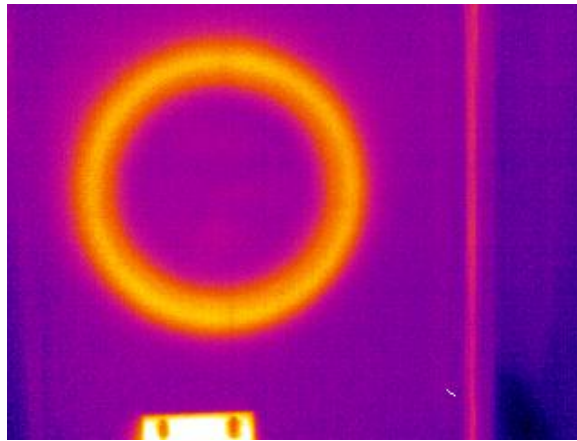


Figure 5-1: thermal image of the TCS heating pattern.

From the first direct measurement of the power density in the heating pattern recently done with an infrared camera, it has been possible to check that the real power distribution on the test mass is well represented by the image taken with the thermal camera on the screen. So, we used this as the input to perform thermal analysis with ANSYS. Figure 5.2 shows the thermal profile. Following the same procedure established in section **Error! Reference source not found.**, we estimated with ANSYS the strength of the lens due to the CO₂ ring. The result gives (-42750 ± 4) m/W (see Figure 5.3).

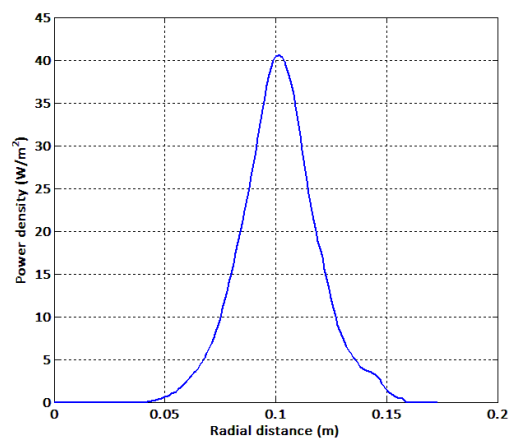


Figure 5.2: heating profile used in thermal simulations

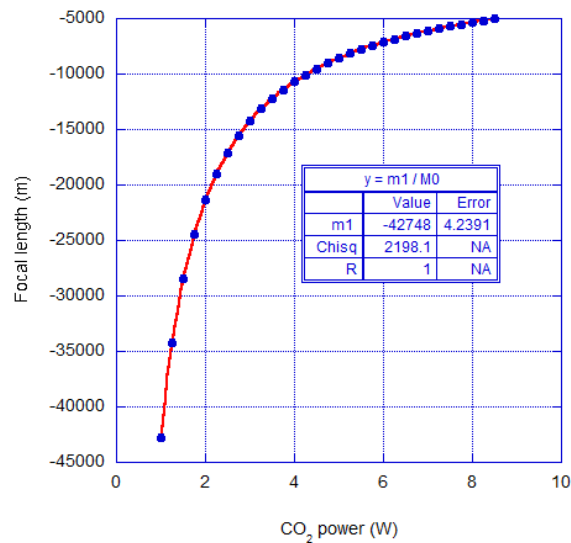


Figure 5.3: focal length of the TCS beam as a function of the CO₂ power

5.2. Comparison of ANSYS results with phase camera measurements

As reported in section 4, the best tuning with 17W input power was achieved with 6.5W on the WI and 4W on the NI (see Figure 4.4). TCS powers have been optimized within 0.5W. We can use this result to estimate the absorptions of the two mirrors. In fact, considering coupling losses [9] as a figure of merit for the TCS, it is found that for a given absorbed YAG power, the coupling losses are a function of the CO₂ power. We looked for the value of the absorptions that minimizes the coupling losses for the optimized TCS powers. The result, shown in Figure 5.4, gives (3.5±0.5) ppm for the NI and (5.4±0.5) ppm for the WI. The coupling losses corresponding to the optimized TCS power are about 400 ppm and 900 ppm for the NI and WI respectively.

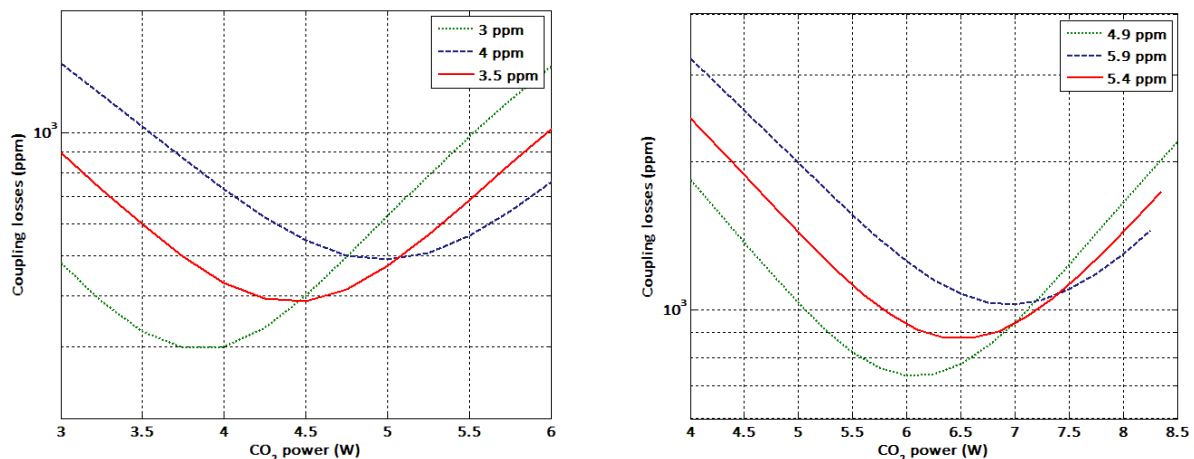


Figure 5.4: coupling losses as a function of the TCS power. A minimum is reached at 4.5W for 3.5 ppm of coating absorption (left image) and at 6.5W for 5.4 ppm (right image). The green and blue curves correspond to the optimized power ± 0.5W.

The residual focal length, computed as described in section 2, is 58 km for 3.5 ppm and 38 km for 5.4 ppm coating absorptions. These values are compatible with those estimated in section 4, since both the phase camera and Finesse cannot distinguish focal lengths larger than 40 km.

6. BS pick-off beam size and phase camera measurements

6.1. Introduction

In the preceding chapters the thermal lensing induced in the Fabry-Perot input mirrors has been estimated by observing the behavior of the locked interferometer. In chapter 3 this was done by measuring the optical transfer function and comparing with interferometer simulations. In chapter 4 this was done by observing the upper and lower sideband amplitude distribution in the dark port and, again, comparing with interferometer simulations. Both techniques have in common that they must simulate a complex system in order to deduce the thermal lensing of the input mirrors. In addition they give an “average” lensing and are unable to determine quantitatively the lensing in each individual input mirror.

In this section we will present two methods of measuring directly the thermal lensing in each input mirror by means of an optical measurement. Both measurements are made on the B1p beam which is on the dark fringe before the OMC. The first method is by using the newly installed phase camera 1. The second method looks at the spot size in the B1p camera.

6.2. Phase camera measurement

The principal objective of the phase camera is to be able to independently measure the spatial distribution of the carrier, lower sideband and upper sideband. A schematic setup is shown in figure 6.1.

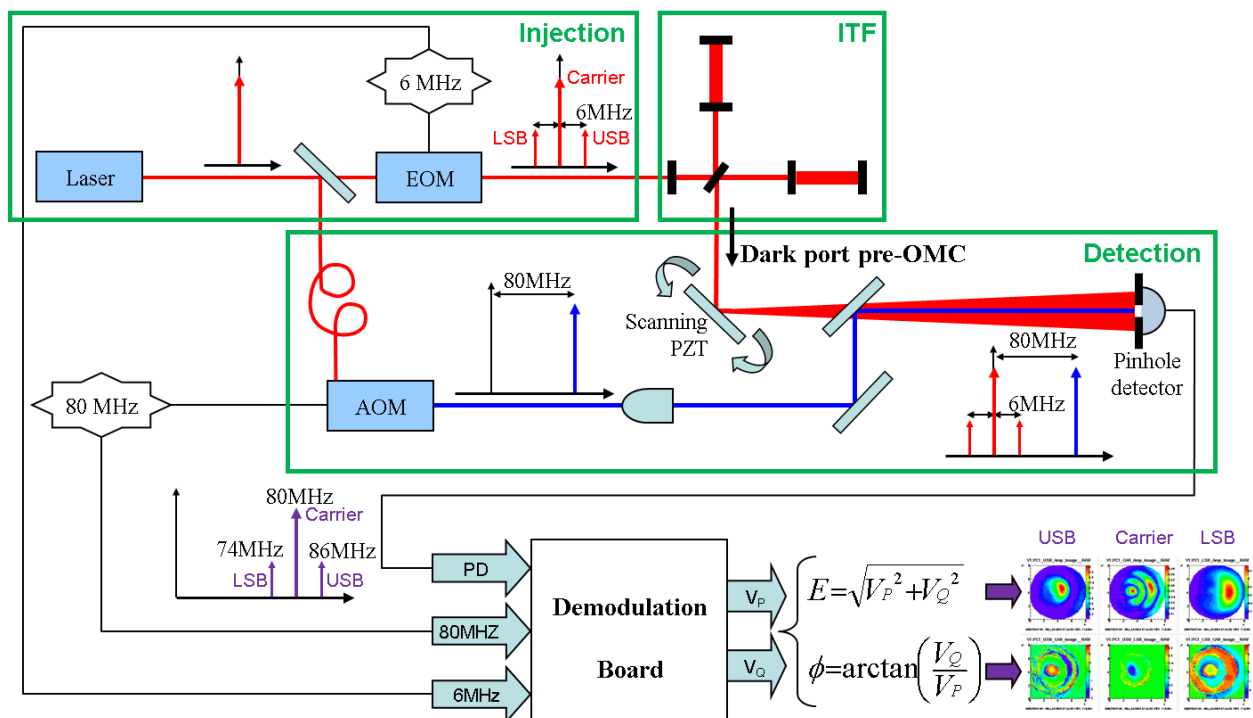


Figure 6.1: Schematic setup of Phase Camera 1 in Virgo+.

The beam to be measured, containing the carrier and two sidebands at ± 6 MHz is scanned over a pinhole detector using a mirror mounted on a 2-axis piezo-electric actuator. At the detector the beam is mixed with a reference beam which has been sampled from the injection bench before the

6MHz phase modulation and then shifted in optical frequency by 80MHz using an acousto-optic modulator. The mixing results in beat frequencies of 74, 80 and 86MHz corresponding respectively to the lower sideband, carrier and upper sideband. Each of these signals is demodulated yielding a signal in phase V_P and a signal in quadrature V_Q . From these signals the amplitude E and phase ϕ of the three fields may be directly calculated by $E = \sqrt{V_P^2 + V_Q^2}$ and $\phi = \arctan\left(\frac{V_Q}{V_P}\right)$.

Up until now, and as we saw in chapter 4, it is the amplitude images of the phase camera that have been used to qualitatively assess the thermal effects on the sidebands. In this chapter we will try to use the phase information in order to measure the wavefront of the beam and to determine quantitatively the thermal effects in the input mirrors.

Two measurement configurations were tried, which are shown in figure 6.2.

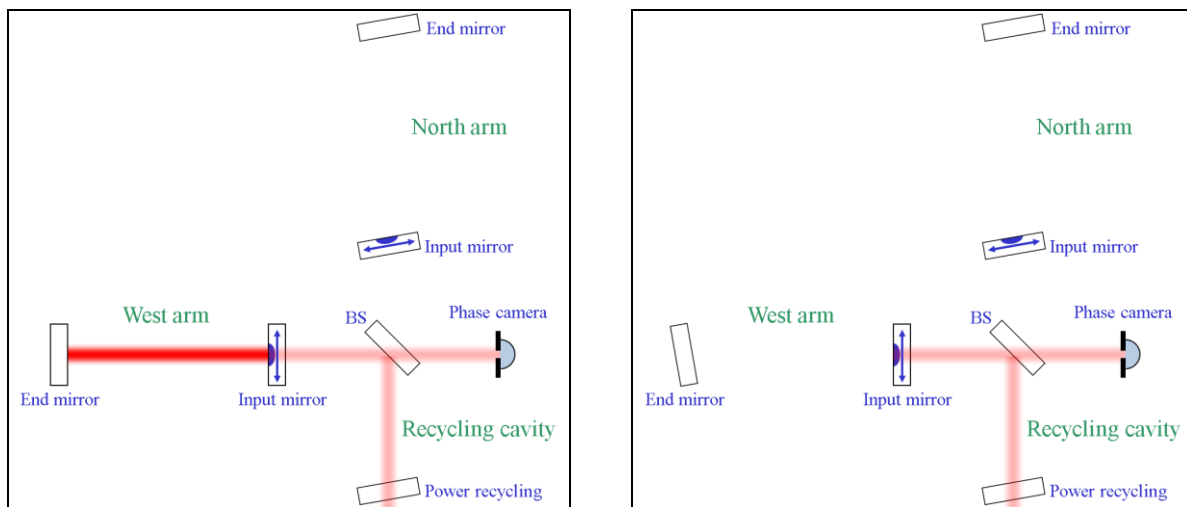


Figure 6.2: Two measurement configurations. A) (Left), West arm locked. B) (Right), West arm unlocked but West input aligned.

This figure shows the two possible configurations for measuring, for example, the thermal effects in the West input mirror.

6.2.1. Configuration A:

In the first configuration the West arm is locked and everything else is misaligned apart from the beamsplitter. Simulations in DarkF [6] and Finesse have shown that the carrier wavefront reflected from the arm cavity is unaffected by thermal effects in the input mirror while the sidebands, that are not resonant in the cavity, have their wavefront deformed proportionally to the change in optical path length in the input mirror substrate due to thermal effects. Therefore the difference between the carrier phase image and the sideband phase image yields directly a measurement of thermal lensing. It is important to note that, in order to measure correctly the wavefront deformation due to the input mirror, the phase camera must be at the same gouy phase as the input mirror. This was achieved with an estimated accuracy of ± 4 deg (log entry 21674). Figure 6.3 shows a result using this configuration while heating the center of the input mirror with a CO₂ beam of roughly the same size as the YAG beam. The amplitude image on the left gives no information about thermal effects as the recycling cavity is not locked. However in the image showing the difference in phase between carrier and lower sideband we see clearly the thermal lensing due to the absorption of the CO₂ beam. This first configuration gives the advantage of being less sensitive to vibrations and length noise due to the differential phase measurement. Tentative measurements were made using this method [7]. However it proved difficult to maintain

a stable lock of the arm cavity. In addition we assume that the carrier wavefront remains unchanged throughout the experiment which could not be confirmed. For these reasons most of the results were taken using configuration B.

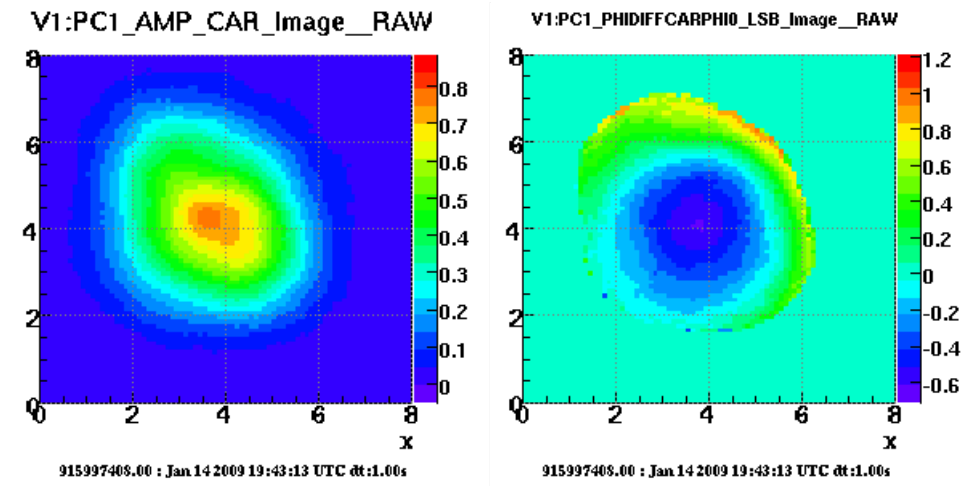


Figure 6.3: Carrier amplitude (left) and carrier – lower-sideband phase difference(right) in reflection of arm cavity the input mirror of which is being heated by the CO2 central spot. Color scale for phase in radians.

6.2.2. Configuration B:

This configuration is much simpler consisting of measuring the phase of either the carrier, upper sideband or lower sideband in reflection of the input mirror. Any change in the wavefront shape should, in theory, be attributed to thermal effects in input mirror being used. Unlike the configuration A, an absolute measurement of the phase is made which leads to a number of issues. A high phase gradient in the phase images leads to high coupling of phase camera PZT position sensor noise (logbook 22161). In addition an entire phase image is captured in two seconds making the measurement extremely sensitive to phase noise caused by vibrations and “swinging” mirrors and benches. In order to minimize the problems of phase noise two modifications were made for

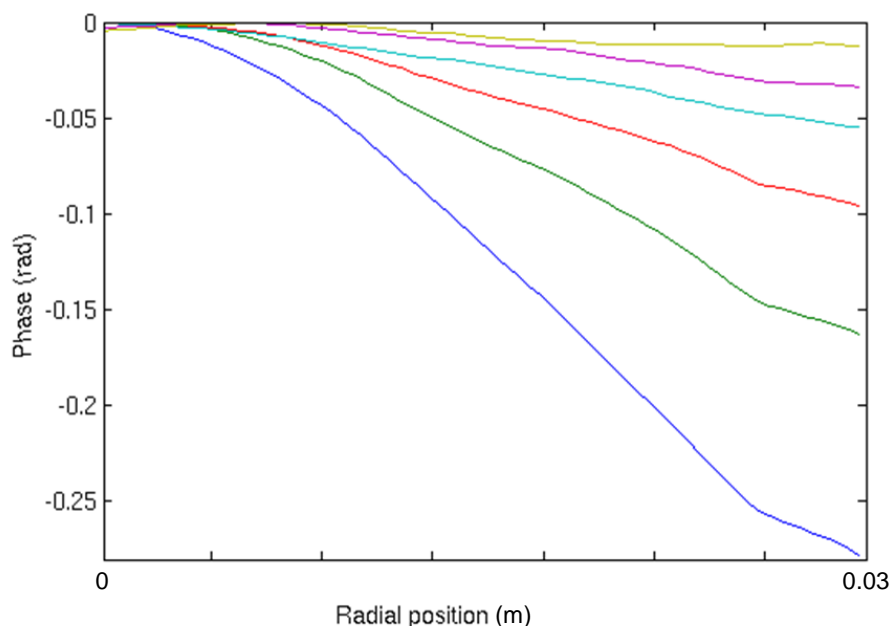


Figure 6.4: Phase profile of wavefront measured by phase camera of cooling mirror that was heated by an 83mW CO2 central spot. Hot mirror (blue) through to cold mirror (yellow).

this configuration. The first was to add a “single-point” detector on the same bench as the phase camera. The signal from this detector, which is effectively a one pixel phase camera, would be demodulated in the same way as the phase camera and its phase used as a reference in order to reduce phase noise. The second modification was to carry out line scans instead of image scans. This increased the scan rate from 0.5Hz to 50Hz allowing to be insensitive to low frequency noise and reduce high frequency noise by averaging. Figure 6.4 shows the wavefront profile of the cooling input mirror which was heated at the centre by an 83mW±10% CO2 laser beam. The sensitivity is much greater with respect to configuration A.

6.2.3. Measuring Thermal Lens

In order to calculate the effective thermal lensing a quadratic fit of the phase profile is made which is weighted by the YAG beam intensity. The thermal lensing is given as a focal length in meters or as a lens power in dioptres (1/m) and corresponds to a single pass through the thermal lens (the raw phase camera result corresponds to a double-pass through the thermal lens). Figure 6.5 shows the thermal lensing measured when a CO2 beam heats up the centre of the Fabry-Perot input mirror. The repeatability of the lensing measurement with a 1sec integration time is found to be 5e-6 dioptres which corresponds to a focal length of 200km.

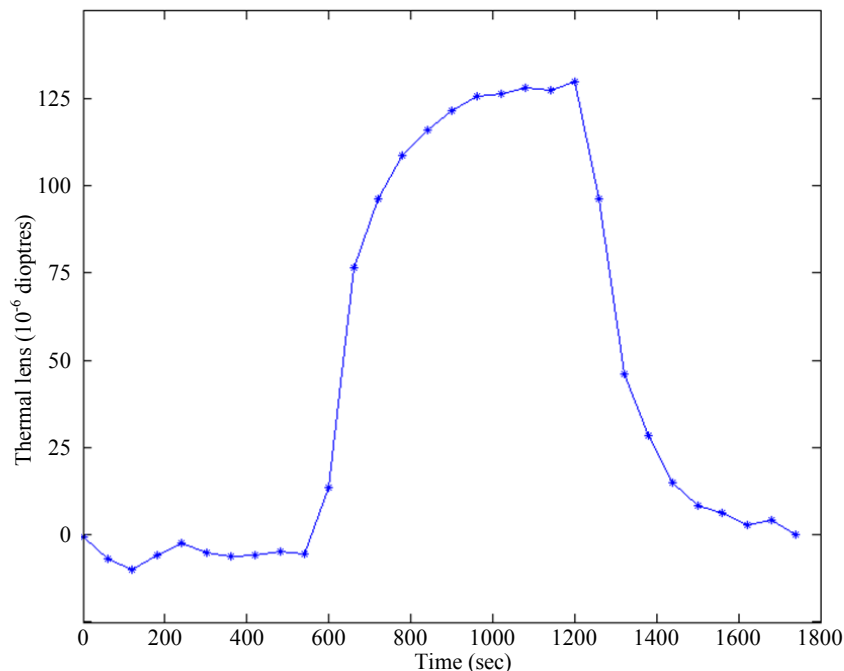


Figure 6.5: Thermal lens measured in North input mirror using phase camera. 90mW CO2 central spot switched on at t=600 sec then off at t=1200 sec.

6.2.4. ITF cool-down to determine input mirror lensing

Both measurement configurations give a thermal lens measurement that is relative. Therefore in order to measure the lensing of the ‘hot’ input mirrors we must make a measurement of the mirror

in both the hot and cold state. The measurement technique consists of locking the entire interferometer such that the input mirrors reach their ‘hot’ state. The interferometer is then unlocked and the mirrors are ‘quickly’ aligned according to the measurement configuration for one of the two input mirrors. We then measure the lensing of the input mirror as it cools down. Figure 6.6 shows the result of such an experiment carried out for both the North and West input mirrors with an input laser power of 17 W. By setting the cold state lensing to zero and extrapolating the graphs to ‘time = 0’ we may estimate the hot input mirror lensing to be:

North input lensing = $35 \cdot 10^{-6}$ dioptres $\pm 29\%$ \rightarrow focal length = 29 km

West input lensing = $27 \cdot 10^{-6}$ dioptres $\pm 29\%$ \rightarrow focal length = 37 km

The attributed errors are obtained by estimating a calibration error of 20%, an error in extrapolating to time=0 of 15% and a statistical error of $5 \cdot 10^{-6}$ dioptres.

This result suggests that the thermal lensing is 30% greater in the North input than the West input.

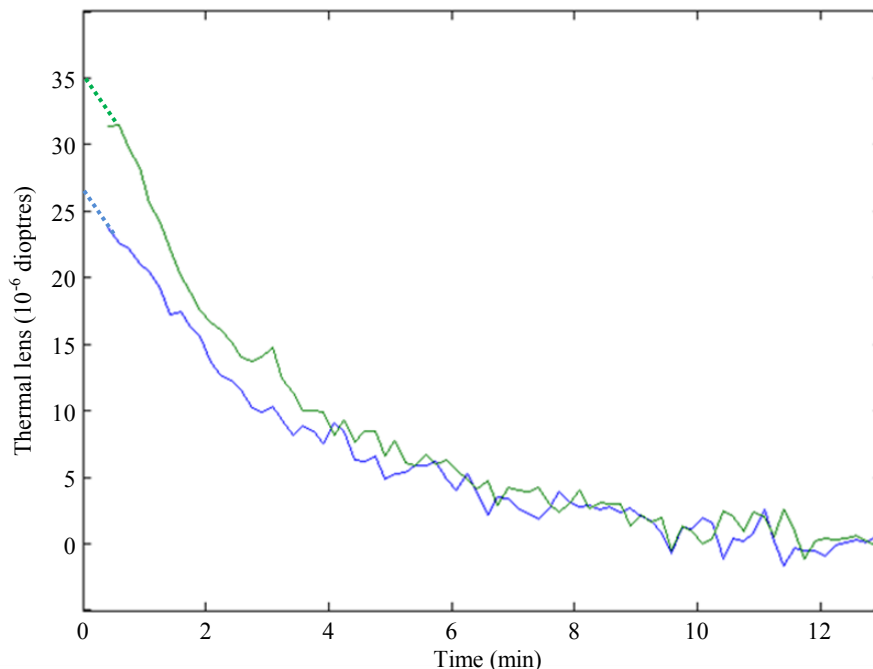


Figure 6.6: Thermal lens measured for input mirrors North (Green) and West (Blue) after ITF unlock. Dotted lines are extrapolations to time of unlock. Input laser power is 17W.

6.2.5. Calculating absorption.

Now that we have a measurement of the lensing we may calculate an estimation of the absorption of the mirror coating. This calculation is presented graphically in figure 6.7.

In order to convert the thermal lensing into power absorbed we use results from the thermal simulations of absorption in the coating of the input mirrors. These simulations yield a lens constant of $2.6 \cdot 10^{-3} \pm 10\%$ dpt/W (see chapter 2). The absorption in ppm is calculated using a cavity power given by:

$$P_{cav} = \frac{P_{in} G_{rec} \mathcal{F}}{\pi}$$

where $P_{in} = 17W \pm 5\%$ is the input laser power, $G_{rec} = 45 \pm 10\%$ [8] is the recycling gain and $\mathcal{F} = 50 \pm 15\%$ is the arm cavity finesse..

The calculated absorption coefficients using the phase camera measurements are therefore:

North input absorption = 1.10 ppm±36%

West input absorption = 0.85 ppm±36%

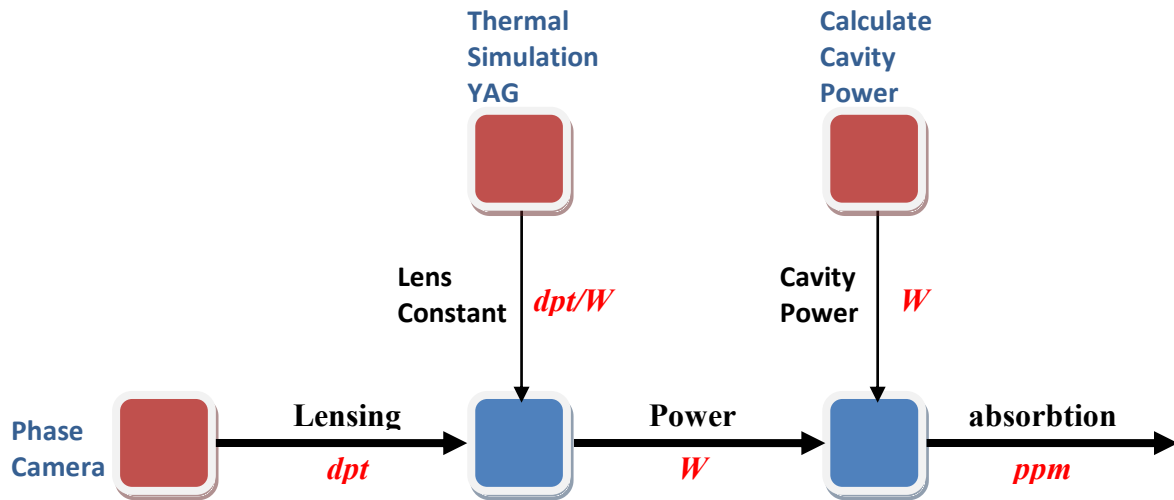


Figure 6.7 : Flow chart showing calculation of absorption from phase camera measurement.

One limitation of this measurement is that no explicit calibration has been made of the phase camera. This could be done in future work using a commercial wavefront sensor.

6.3. Beam Size Measurement.

The phase camera, which is placed on the B1p beam, is in the same Gouy phase as the input mirrors and measures directly the modification of the wavefront shape. The traditional CCD camera that is installed on the B1p beam is at a different Gouy phase. Therefore a modification of the wavefront due to thermal lensing in the input mirror will result in a change in size and shape of the beam on the B1p CCD camera. In this section we will see how the measurement of the beam size at the B1p CCD camera may be used to measure the lensing in the input mirrors.

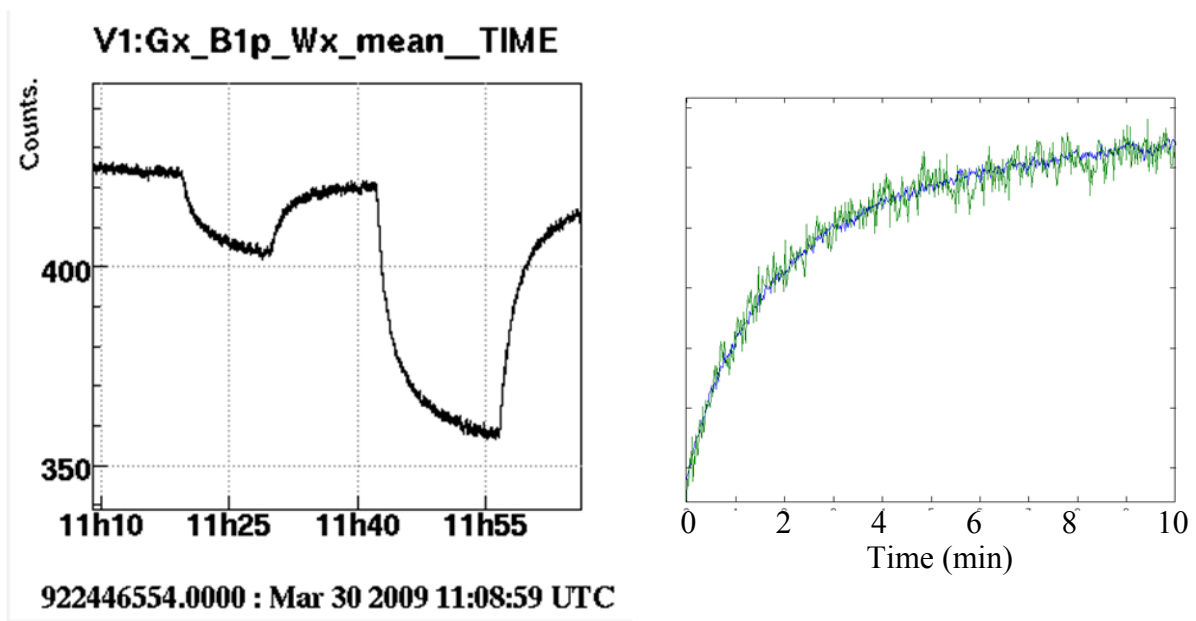


Figure 6.8: Thermal lens measured in North input mirror using B1p camera. Left: 23mW & 83mW CO2 central spot respectively switched on then off. Right: Superposition of 23mW & 83mW CO2 central spot cool-down using a scaling factor of 3.4.

The measurement configuration is the same as that of configuration B used for the phase camera measurements. Figure 6.8 shows CO₂ central spot cool-down tests made on the North input using the data channel Gx_B1p_Wx which gives the beam size in the x axis on the camera B1p. We see clearly that the positive lens generated by the central spot results in a reduction in spot size at the B1p camera. In order to test the linearity of this method for measuring thermal lensing, this cool-down test was carried out for a CO₂ power of both 23mW and 83mW. The right hand side of figure 6.8 shows the superposition of the two cool-down tests with a scaling factor of 3.4. This scaling factor is very close to $83mW/23mW = 3.6$ and therefore gives a confirmation that beam size is proportional to thermal lensing in the input mirror.

6.3.1. Calibrating with CO₂ ring

In order to measure quantitatively the thermal lensing with camera B1p it is necessary to calibrate the system. This is done by creating a ‘known’ thermal lens and observing the change in beam size. This thermal lens is generated by shining a known CO₂ ring power onto the input mirror and using thermal simulations to calculate the induced thermal lens. On the right of figure 6.9 we see the experimental and simulated CO₂ ring cool-down test. We see that we are able to predict the over-shoot in lensing as the input mirror cools down. On the left of the figure we see a flow chart illustrating the calibration of the B1p camera, where W_{CO_2} is the CO₂ laser power, dpt is the lens power and s is the beam size on the B1p camera. The thermal simulation gives a CO₂ ring lens constant of $-3 \cdot 10^{-5} \text{ dpt}/W_{CO_2} \pm 10\%$. It is interesting to note that this constant is a factor 87 lower than the YAG lens constant demonstrating that it is much less power efficient to generate a negative lens. The beam size was found to change as $5.9 \text{ s}/W_{CO_2} \pm 16\%$. This yields a camera calibration constant of $-5.1 \cdot 10^{-6} \text{ dpt}/s \pm 19\%$.

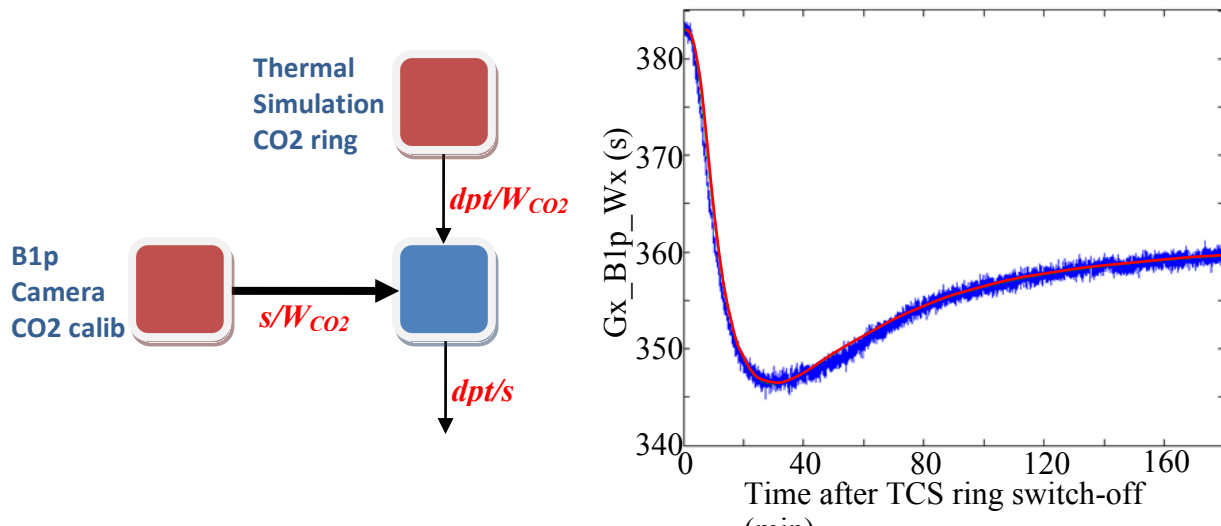


Figure 6.9 : Left: Flow chart showing calibration of B1p camera calibration. Right: cool-down test with 4W CO₂ ring on North input (blue) compared with lens power calculated from thermal simulation (red).

6.3.2. ITF cool-down to determine input mirror lensing

The procedure for measurement of the thermal lens in West input and North input by ITF cool-down is essentially the same as that of the phase camera cool-down measurement in section 6.2.4. The left of figure 6.10 shows the raw data of the cool-down measurement of West and then of North input. The right of figure 6.10 shows the superposition of an ITF cool-down and CO₂ central spot cool-down. We see that they both have the same shape apart from the first 20 seconds

after unlock which could be explained by ‘fast’ thermal effects in the injection system due to misalignment of the PR consequently changing the Faraday isolator lensing. Analysis of the results yields an estimated change in beam size of $19s \pm 20\%$ for West input and $22s \pm 20\%$ for North input. Using the calibration made in the previous section we may therefore estimate the hot input mirror lensing to be:

North input lensing = $112 \cdot 10^{-6}$ dioptres $\pm 28\%$ \rightarrow focal length = 8.9 km

West input lensing = $97 \cdot 10^{-6}$ dioptres $\pm 28\%$ \rightarrow focal length = 10.3 km

This result suggests that the thermal lensing is 15% greater in the North input than the West input.

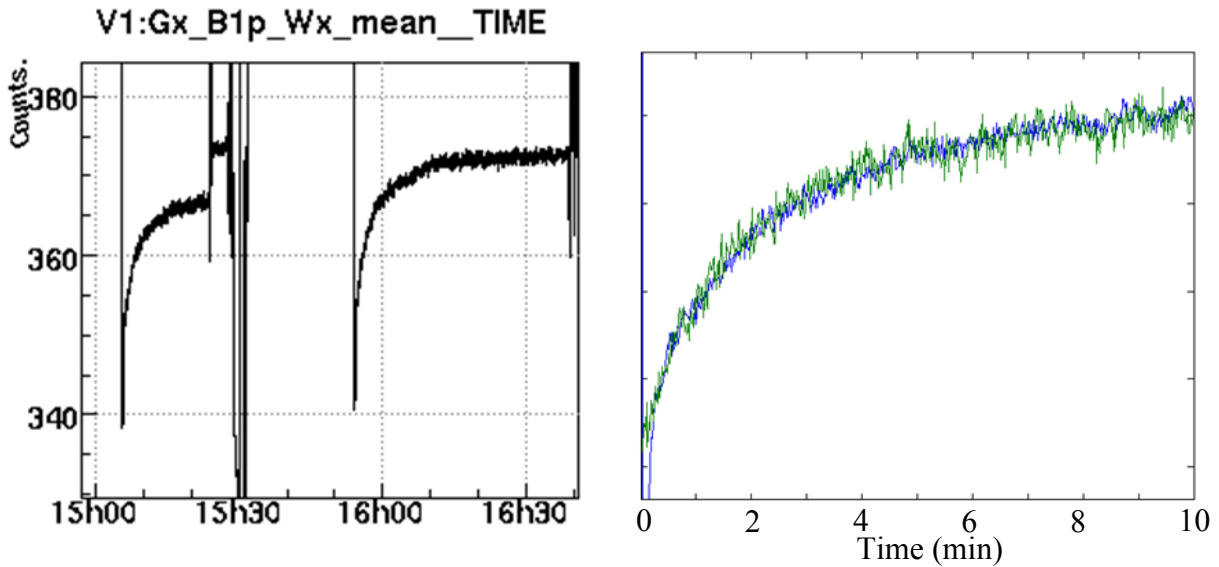


Figure 6.10: Left: ITF cool-down measurement for West input mirror followed by North input mirror. Right: Superposition of West input ITF cool-down (blue) & 23mW CO2 central spot cool-down (green) using a scaling factor of 1.16

6.3.3. Calculating absorption.

We may now proceed in the calculation of absorption as we did in section 6.2.5. The flow chart for the complete calculation from beam size to absorption is given in figure 6.11.

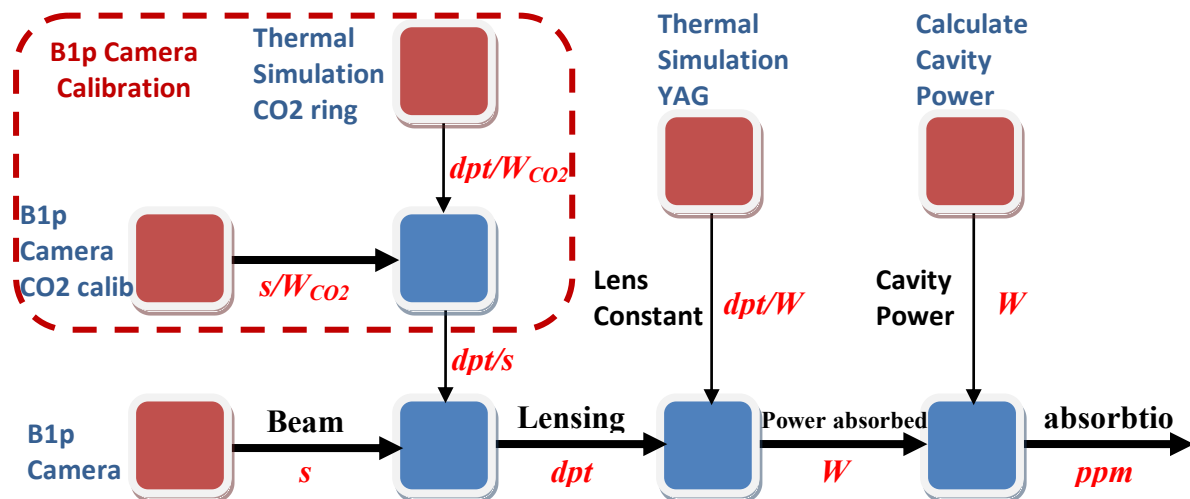



Figure 6.11 : Flow chart showing calculation of absorption from beam size measurement.

	<p style="text-align: center;">VIRGO NOTE Virgo Input Mirrors thermal effects characterization</p>	<p>Date 17/03/2010 VIR-0191A-10 page : Page 23 of 33</p>
--	--	--

The calculated absorption coefficients using the beam size measurements are therefore:

North input absorption = 3.53 ppm±35%

West input absorption = 3.04 ppm±35%

6.4. Conclusion

In this chapter we have described two independent optical methods to measure directly the thermal lensing in the input mirrors and hence, by comparison with thermal simulation, estimate their absorption. Both techniques give good agreement in the relative absorption of the two input mirrors; the North input absorption is greater than that of West input by 15-30%. However the absolute measurements of absorption differ by more than a factor three. The phase camera measurements are significantly lower than all other results described in this document. This could lead us to believe that there is a fundamental problem with this measurement which therefore requires further investigation.

7. Mirror absorption measurement through the bulk temperature measurement with the resonant mode technique

7.1. The resonant mode method

The measurement of the mirror temperature through the resonant mode technique is simply based on the fact that the elastic properties of the substrate are temperature dependent and each normal mode will drift in frequency if the bulk temperature changes. The first idea to use this method in Virgo has been suggested by M. Punturo and F.Travasso in 2001 and described in the Flavio's thesis. The conversion coefficient ($\text{Hz} \leftrightarrow \text{K}$) is 0.28Hz/K for the Butterfly modes (at about 3.9 kHz) and 0.61Hz/K for the Drum mode (at about 5.5kHz) and it has been computed through an ANSYS finite element model, considering the Suprasil elastic parameters and an uniform temperature distribution in the bulk. This method has been first used in the [C5 analysis](#) to show the temperature increase of the NI mirror due to the loss of the Tx control and consequent variation of the transmitted power due to the etalon effect. Currently (since C5), a monitor is running "in time" (using the data saved on disk in the raw.fl1); it generates the FFT of the dark fringe channel (Pr_B1_ACp) when the OMC is locked, using 540s of data length and 54s of FFT window. The four drum mode peaks and four butterfly mode peaks are detected and the peak frequency reconstructed averaging 3 bins around the absolute maximum. This method reduces but don't eliminate the binning problem due to the fact that the bin size is larger than the thermal peak width (considering a $Q \sim 10^7$). For sake of completeness it should be underlined that, because of the presence of the lateral flats in the suspended mirrors butterfly mode, doublets are expected (and this is the reason why in Figure 7.1 there are two overlapped butterfly mode lines), but, although a longer FFT is realized, no doublet has been identified.

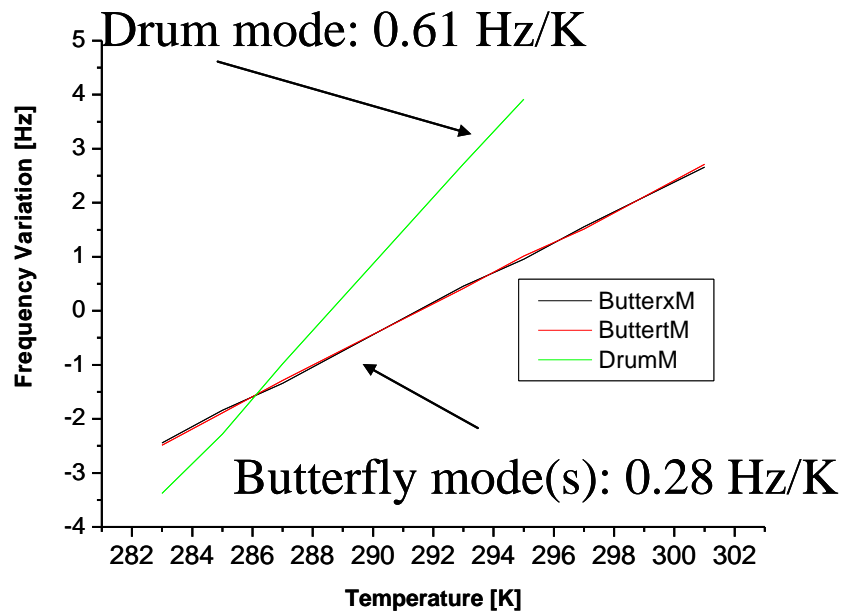


Figure 7.1 - ANSYS simulation of the frequency dependence of the first two resonant modes of the Virgo mirrors. Butterfly mode is at about 3.9kHz and Drum mode at about 5.5kHz

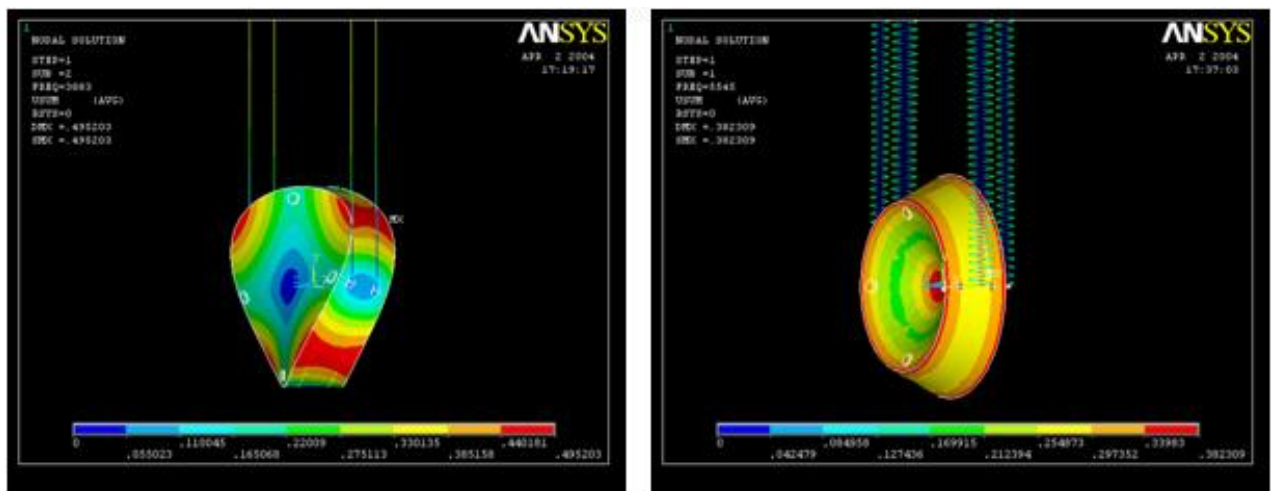


Figure 7.2 - Mirror modes. Left, Butterfly mode at about 3.9kHz; Right, Drum mode at about 5.5kHz

The first step is the identification (“who is who”) of the peaks and their association to the main cavities mirrors. This has been done considering that input and end mirrors have slightly different thickness corresponding to about 40Hz of frequency difference in the drum mode; the distinction WI/NI and WE/NE has been done looking for specific temperature variation driven by TCS actions (in the input mirrors) or environmental temperature variation (in the end). Recently (logbook entries [25836](#) and [26014](#)) it has been shown that the north arm mirrors can be easily distinguished from the west arm mirrors looking at the channel Pr_B5_d2, where the peaks relative to the north arms have a larger amplitude with respect to the west arm mirror resonant modes.

7.2. Verification of the calibration

The identification of the modes through the environmental temperature variation permits also to indirectly verify the Hz \leftrightarrow K calibration coefficient. The latest measurement is in the logbook [entry 26014](#) and the relative plot is shown in Figure 7.3. Obviously the mirror temperature fluctuation reconstructed through the mirror modes are quite similar (this means that the method implementation is correct) but the comparison with the temperature sensors in the channels “Em_TESUNE11 (dTNEF7)” and “Em_TESUNE01 (dTNEF0)” suggests that probably the two probes are swapped. It should be stressed that because of the separating roof and of the height of the tower is not absolutely expected that the mirror temperature exactly follows the tower temperature fluctuation (as underlined by the different behavior of the F7 and F0 temperatures), but the fact that, after 5 months and a seasonal temperature drift of about one degree, the temperature variation difference between the F0 and the mirror is less than 0.1 degree could suggest that the calibration error is surely lower than 10%. A thermometer installed in the reference mass will permit in the future a better estimation of this error.

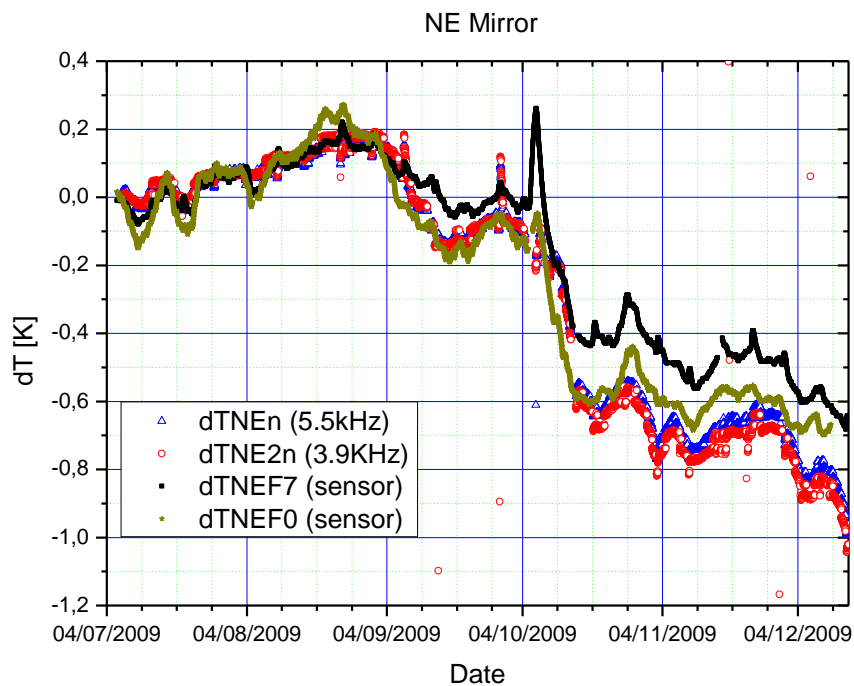



Figure 7.3 - temperature variation in the NE tower during the first 5 months of the VSR2.

Another way to verify the temperature measurement method is given by the etalon effect. Several thermo-optical predictions have been confirmed using the etalon effect in Virgo but the more important is the measurement of the refraction index gradient with respect to the temperature ($\beta = dn/dT$) of the input test masses. The variation of the power transmitted at the end of the Virgo \times arms, given by the etalon effect, permits to evaluate β . The value measured (see entry [22178](#)) is about $7.8 \times 10^{-6} \text{ K}^{-1}$ close to the newest “expected” values for Suprasil in literature¹, confirming the a calibration error lower than 10%.

¹ In literature it is possible to find several discrepant numbers. In the [official Heraeus data sheet](#) it is possible to find the β values only in the $\lambda \in [237\text{nm}, 638\text{nm}]$; in that range β varies in the $[14.6\text{K}^{-1}, 9.6\text{K}^{-1}]$ interval. In an email from Heraeus to Julien Marque they stated about 8.7ppm at 1064 nm, but in another private communication between Heraeus and GEO600 people (http://www.ligo.org/pdf_public/hild01.pdf) they stated $\beta/\kappa = 10^{-5}$ (where $\kappa = 1.38 \text{ Wm}^{-1}$

	<p style="text-align: center;">VIRGO NOTE Virgo Input Mirrors thermal effects characterization</p>	<p>Date 17/03/2010 VIR-0191A-10 page : Page 26 of 33</p>
--	--	--

7.3. Opto-Thermal finite element modeling of the mirror

The second fundamental ingredient to evaluate the absorption through the resonant mode technique is the opto-thermal modeling of the input mirrors. This has been done through a custom FEM² that divides the mirror in rings and slices (having a cylindrical symmetry) and implements all the heat transport laws between the elements. The realization of a custom FEM, rather than a commercial one, has been driven by the need to simulate the behavior of the Virgo cavities miming locks lasting for long time. Thanks to the cylindrical symmetry constrain, this code is largely faster than the commercial products. The accuracy of this code is an important key point. The validity of the code has been verified simulating the whole VSR1 behavior of the Virgo cavities. In Figure 7.4 the comparison between the simulated thermal behavior of the input mirrors and the data measured during VSR1 is performed. The agreement is impressive and also the prediction potential of the code is confirmed by what is described in the Figure 7.4 caption. The temperature variation shown in Figure 7.4 are driven by the environmental temperature fluctuations and they corresponds to a situation where the temperature is uniformly distribute in the input mirrors. What about the accuracy of the prediction in case of a non-uniform temperature field (i.e. caused by the Gaussian Yag beam absorption)? Entries [20446](#) and [22287](#) in the logbook permit to evaluate this situation. In the first entry the cooling of the WI mirror is followed after one of the first TCS tests. The thermal time constant has been evaluate to be about 17000±1300s (G. Vajente recently measured with more precision, about 20000s, entry [25808](#)) that corresponds to an emissivity³ e_M (analytically computed):

$$e_M^{Ana} = \frac{M_M \cdot c_{FS}}{4\sigma_{SB} \cdot S_e T_{room}^3} \cdot \frac{1}{\tau_{cooling}}$$

where σ_{SB} is the Stefan-Boltzmann constant, c_{FS} the specific heat of the mirror of mass M_M , S_e is the total radiating surface and $\tau_{cooling}$, obviously, is the cooling time constant. Analytical computation considers the mirror temperature uniform and results in an emissivity of about 0.56. FEM simulation of the same process gives an emissivity of about 0.53. It should be noted that this value, although within the wide range that it is possible to find in literature⁴, is quite low but its correctness if confirmed in the entry [22287](#) in the logbook, where a warming up event of the NI mirror has been acquired and compared to the simulation, having a perfect agreement if $e_M=0.53$ (see Figure 7.5).

7.4. Absorption measurement

Now we have all the ingredients to compute the mirror absorption. The measurement is calorimetric, based on the warming up of the mirror when illuminated by the Yag beam. In this way the overall mirror absorption is computed without the possibility to distinguish between the substrate, anti-reflective (AR) and high-reflectivity (HR) coatings. To extrapolate the HR coating absorption it has been selected 0.7 ppm/cm of substrate absorption and has been neglected any

¹K⁻¹ is the thermal conductivity) corresponding to $\beta = 13.8 \times 10^{-6}$. Finally in a paper that will be published soon in Applied Optics (Paul-Edouard DUPOUY et al, "[Interferometric measurement of the temperature dependence of an index of refraction: application to fused silica](#)") it has been measured, using an etalon technique, for Suprasil, $\beta/\kappa = (T=25^\circ, \lambda=633\text{nm}) = (8.65 \pm 0.18) \times 10^{-6}$ that, considering the expected decreasing trend passing from visible light to infrared matches with our measurements (that we should publish!)

² Realized in Matlab™ by M.Punturo, modifying a code realized for the Crystal project in Virgo

³ The emissivity e is defined by the Stefan-Boltzman law:

$$i_e = e_M \cdot \sigma_{SB} S_e (T_e^4 - T_{room}^4)$$

⁴ It is possible to find $0.5 \leq e_M \leq 0.98$

absorption in the AR coating but the weight of these choices is rather low because of the finesse enhancement role.

To perform the measurement is needed to find a data period where there are few lock-unlock events, in a quiet ITF condition, with environmental temperature really stable. In fact with about 5kW of power stored in the cavity, neglecting the radiative current, about 0.02 mK/ppm/min of temperature increase rate is expected with an overall warming up measured of the order of 20-30mK. It is quite obvious that the environmental temperature stability plays a dominant role in the measurement error determination and it is impossible to base a measurement of the absorption in a single or two measurements. For this reason the statistical error in the measurement of the absorption with this method is quite large, but also other systematic errors enter in the evaluation. Collecting all the best data in the VSR1 and commissioning period (all the data successive to the TCS installation cannot be used for this purpose, since mirror temperature is determined by the TCS laser beam power), the final measurement on the input mirrors absorption are reported in the following table

Table 7.1- Coating absorption in the input mirrors

Mirror	HR coating absorption (ppm)	Statistical error (ppm)
NI	4.6	1.0
WI	5.6	2.5

The evaluation of the systematic errors is made in the entry [17382](#) in the logbook. An incertitude of the $\pm 5\%$ in the IMC output power causes an error of ± 0.23 ppm, meanwhile the optical gain fluctuation given by the etalon effect (since the nominal finesse has been used in the computation) causes a ± 0.15 ppm of error. A recycling gain of 45 has been considered, with an incertitude of 10% leading to ± 0.5 ppm. Finally, a 9% of calibration error causes a ± 0.38 ppm of systematic incertitude.

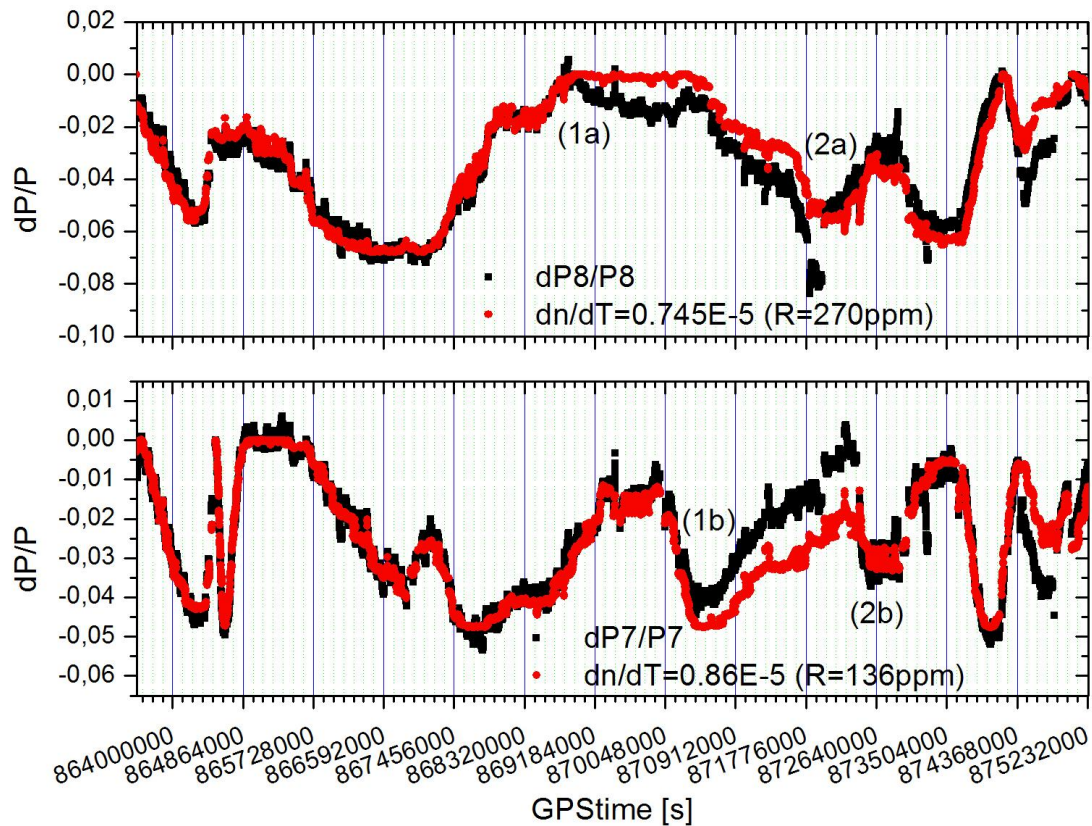


Figure 7.4 - Power transmitted at the end of the West (upper panel) and North (lower panel) arms. Black curves represent the acquired photodiodes output (normalized by B5) and the red curves are the simulated data. The total data stream represents more than 130 days during VSR1. Values adopted for b are different from what reported in this note since an old (and incorrect) model was used at that time (see entry [22178](#) in the logbook). Simulation agrees perfectly with the measured data, except in the intervals [1a,2a] and [1b,2b]. In this case the model is correct, but the data acquired are spoiled by the misalignment of the photodiodes in the end benches as described in the entries [18332](#) and [18390](#) in the logbook; when the end benches are re-aligned (points 2a and 2b) the discrepancy disappears.

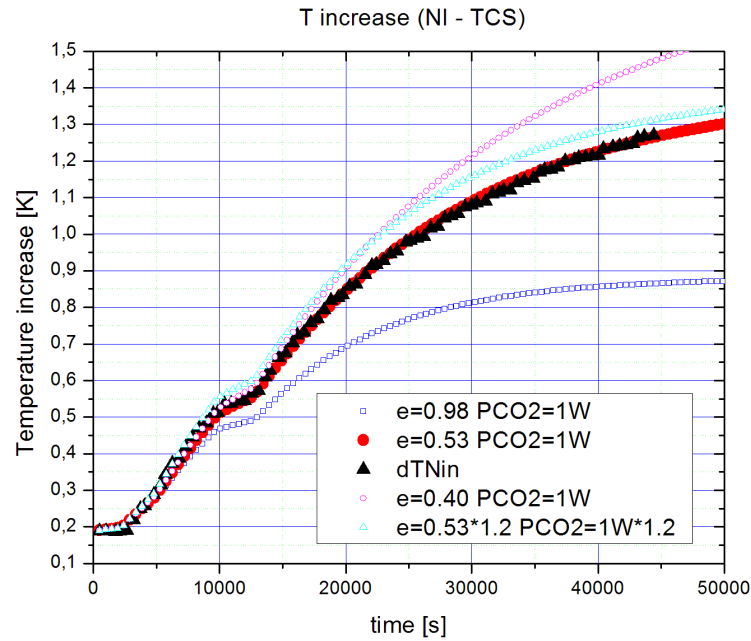


Figure 7.5 - NI mirror warming up caused by 1W in the TCS. Black triangles are the acquired data and the other curves are related to the simulation with different emissivity (e) and different input power. The good agreement with $e_M=0.53$ is evident.

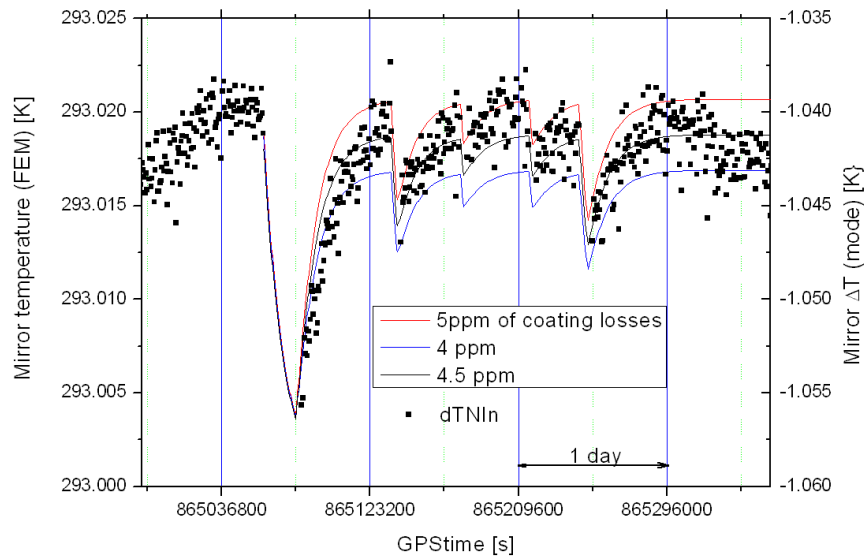


Figure 7.6 - lock-unlock cycles permitting to measure the coating absorption


8. Conclusions

Before transportation to the Virgo site, the absorption of the HR coating of the Virgo IMs has been measured by LMA. The absorption measured was 1.25ppm +/-8% and 1.2ppm +/-17%, respectively for the NI and WI mirrors.

All the measurements done on the site, once the mirrors installed in the towers, are reported below (the error bar is the quadratic sum of all statistical and systematic errors):

Kind of measurement	Mirror	HR coating absorption (ppm)	Error bar
SSFS TF measurement fit with simulation with 8W input and no TCS	IM average	4.7	25%
SSFS TF measurement fit with simulation with 17W input and 3.5W average TCS	IM average	3.2	41%
SSFS TF measurement @ 50kHz fit with simulation with 17W input and 1W average TCS	IM average	2.9	29%
Recycling Side-Bands amplitude shape fit with simulation with 13W input and no TCS	IM average	5.3	32%
Recycling Side-Bands amplitude shape fit with simulation with 17W input and 4+6.5W TCS	NI	3.6	31%
	WI	5.8	31%
Coupling losses minimization with simulation with 17W input and 4+6.5W TCS	NI	3.5	14%
	WI	5.4	14%
Wavefront profile measurement with Phase Camera	NI	1.1	36%
	WI	0.85	36%
Dark fringe spot size measurement	NI	3.5	35%
	WI	3	35%
Bulk temperature measurement with the resonant mode technique	NI	4.6	26%
	WI	5.6	47%

Even though the statistical error is rather large for many of the measurements, apart from the measurement using the phase profiles of the Phase Camera, all measurements points an absorption of around 4ppm, far from the 1.2ppm measured in LMA after coating deposition. This clearly indicates an important additional absorption of the coatings after installation. The only hypothesis raised so far to explain this discrepancy was an extra absorption caused by some pollution at the surface of the mirror. As the mirrors have been now dismantled, this will be checked soon thanks to a new measurement in LMA.

	<p style="text-align: center;">VIRGO NOTE Virgo Input Mirrors thermal effects characterization</p>	<p>Date 17/03/2010 VIR-0191A-10 page : Page 31 of 33</p>
--	--	--

9. References

- [1] Jean-Yves Vinet, "On Special Optical Modes and Thermal Issues in Advanced Gravitational Wave Interferometric Detectors", Living Reviews in Relativity (1433-8351), <http://relativity.livingreviews.org/Articles/lrr-2009-5/>
- [2] G. Vajente and J. Marque, "Simulation of SSFS transfer function" (23/01/09, Virgo logbook 21809)
- [3] J. Marque, "SSFS optical TF and Input Mirrors absorption" (10/03/09, Virgo logbook 22322 and 22325)
- [4] J. Marque, "SSFS optical TF" (19/06/09, Virgo logbook 23301)
- [5] J. Marque, "Characterisation of ITF common optical parameters with SSFS TF measurement around 50kHz" (12/11/09, Virgo logbook 25610)
- [6] R. Day, TCS Test and Calibraton meeting, Cascina, TDS Code VIR-0336A-08
- [7] Day, Huet, Rocchi, Marque, Virgo logbook, 21763
- [8] Marque, Virgo logbook, 24927
- [9] J-Y. Vinet, "[On thermal issues in advanced Gravitational Wave Interferometric detectors](#)", TCS workshop, Cascina October 2008

10. Annex

Parameter	Value	Description	Units	Source
SB	5.670400e-8	Stefan-Boltzmann constant	W m ⁻² K ⁻⁴	NIST CODATA
Lambda	1.064e-6	laser wavelength	m	-

Table1: General parameters

Parameter	Value	Description	Units	Source
Diameter	0.35	WI&NI diameter	m	LMA measurement
Thickness	0.097	WI&NI thickness	m	LMA measurement
Tmirror	293	In vacuum mirror temperature	K	Temperature probe on filter 7

Table2: Mirror parameters


Parameter	Value	Description	Units	Source
FS.density	2.20e3	Density	kg m ⁻³	Heraeus
FS.k	1.38	Thermal conductivity	W m ⁻¹ K ⁻¹	Heraeus
FS.c	772	Specific heat	J K ⁻¹ kg ⁻¹	Heraeus
FS.alpha	0.51e-6	Thermal expansion coefficient	K ⁻¹	Heraeus
FS.Poisson	0.170	Poisson ratio	-	Heraeus
FS.Young	70.0e9	Young's modulus	N m ⁻²	Heraeus
FS.emissivity	0.53	Emissivity	-	M. Punturo measurement (logbook 20446 and 22287)

Table3: Fused Silica parameters

Parameter	Value	Description	Units	Source
FS.n	1.44963	Refractive index	-	Heraeus
FS.dndT	8.7e-6	Thermo-optic coefficient	K ⁻¹	Heraeus private communication
FS.abs_pcm	0.6e-6	Bulk absorption per cm	cm ⁻¹	LMA measurement

Table4: Coating optical properties at 1064nm

Parameter	Value	Description	Units	Source
FS.abs.coef_CO2	29.4	absorption coefficient @25C	cm ⁻¹	McLachlan & Meyer, Applied Optics, Vol 26

	<p style="text-align: center;">VIRGO NOTE Virgo Input Mirrors thermal effects characterization</p>	<p>Date 17/03/2010 VIR-0191A-10 page : Page 33 of 33</p>
--	--	--

				No. 9, 1987
FS.ext.coef_CO2	0.025	extinction coefficient @25C	-	McLachlan & Meyer, Applied Optics, Vol 26 No. 9, 1987

Table5: Fused silica optical properties at 10.6 um